

SMALL-SCALE STRUCTURE IN THE $\text{Ly}\alpha$ FOREST AT HIGH REDSHIFT

C. E. PETRY AND C. D. IMPEY

Steward Observatory, University of Arizona, Tucson, AZ 85721; cpetry@as.arizona.edu, cimpey@as.arizona.edu

AND

C. B. FOLTZ

Multiple Mirror Telescope Observatory, University of Arizona, Tucson, AZ 85721; cfoltz@as.arizona.edu

Received 1997 April 25; accepted 1997 September 17

ABSTRACT

We have obtained spectra of the four components of the system B1422+231 with *HST*'s Faint Object Spectrograph in order to study spatial inhomogeneities and velocity variations in the absorbers which are pierced by the four lines of sight. The four images are well resolved, and the spectra clearly show the system is a lensed quasar; a new redshift based on the $\text{Ly}\alpha$ and N v emission lines is measured to be 3.6261. The following are results from the analysis of the four individual lines of sight that probe redshifts $2.9 \leq z \leq 3.5$ and transverse dimensions 0–0.14 h_{100}^{-1} kpc: (1) In the region between $\text{Ly}\beta$ and $\text{Ly}\alpha$ (less 6000 km s^{-1} to allow for the proximity effect: 4745–5511 Å), the limiting rest equivalent width ($1\sigma_{\text{lim}}$) is measured to be 0.059, 0.052, 0.034, and 0.22 Å for components A, B, C, and D, respectively. (2) The total number of $5\sigma_w$ lines found in this region are 83, 85, 102, and 44 for A–D, respectively; for A–C 11, 9, and 13 are identified with metal line systems and the remaining 72, 76, and 89 are assumed to be $\text{Ly}\alpha$ lines. Between paired lines of sight A and B to C, and A paired to B, there are 62, 68, and 62 coincidences and 3, 1, and 1, anticoincidence for the $\text{Ly}\alpha$ lines. For the metal lines there are 8, 9, and 8 coincidences for AC, BC, and AB, respectively, and each has one anticoincidence. (3) Scatter plots of the equivalent widths for the coincident lines for both $\text{Ly}\alpha$ and metals are highly correlated and all pairs match within 100 and 75 km s^{-1} , respectively. (4) Maximum-likelihood analysis limits spatial inhomogeneity for $\text{Ly}\alpha$ absorbers in components A, B, and C to no more than $\sim 15\%$ of the equivalent width of an average ($W = 2$ Å) line. This corresponds to a limit on the mean variation in column density, assuming unsaturated lines, of $\log(\Delta N_{\text{H}}) = 13.1 \text{ cm}^{-2}$. (5) A method of detecting spatial inhomogeneities independent of continuum-fitting and line-profile measurement is developed yielding an upper limit on the column density difference for unsaturated lines of $\log(\Delta N_{\text{H}}) = 12.8$. This is approximately a factor of 2 smaller than the limits obtained from the line pairs. (6) The distribution of the velocity differences for AC, BC, and AB for the $\text{Ly}\alpha$ lines and the metal line pairs have a mean close to zero and rms $\sim 40 \text{ km s}^{-1}$. Maximum-likelihood analysis gives an upper limit on the variations in velocity of $\sim 40 \text{ km s}^{-1}$ for $\text{Ly}\alpha$ absorbers in paired lines of sight. The overall result of this work is a set of stringent limits on the inhomogeneity of low column density hydrogen absorbers on subkiloparsec scales at high redshift.

Subject headings: quasars: absorption lines — gravitational lensing — quasars: individual: (B1422+231)

1. INTRODUCTION

Quasar spectra are powerful diagnostics of the intervening luminous and dark matter in the universe. The abundance of narrow absorption lines in the region blueward of $\text{Ly}\alpha$ emission, the $\text{Ly}\alpha$ “forest,” is due to intervening material distributed along the line of sight. The absorbers have been traditionally divided into two classes—intergalactic hydrogen absorbers presumed to be of primordial abundance (Sargent et al. 1980) and highly ionized species of heavy elements that are associated with galaxy halos (see, e.g., Lanzetta & Bowen 1990; Bergeron & Boisse 1991). Recent high-resolution observations have blurred the distinctions between these two populations. In particular, the hydrogen lines of the $\text{Ly}\alpha$ forest show widespread but weak metal enrichment (Songaila & Cowie 1996; Tytler 1995), and they exhibit significant small-scale velocity clustering ($\Delta v < 300 \text{ km s}^{-1}$) along the line of sight.

Gravitationally lensed quasars provide unique probes of the $\text{Ly}\alpha$ absorbers because light from the separate images follows different paths through the universe, sampling material on transverse scales that depend on the geometry of the system. Estimates of the sizes of the $\text{Ly}\alpha$ absorbers

may be made using the number of coincident and anti-coincident absorption features between the lines of sight, and information about the structure of the absorbers may be inferred by comparing the equivalent widths and velocity separations of the coincident lines. Because the image separations for these systems are typically small ($\Delta\theta \lesssim 3''$), the different lines of sight will sample the same structure at transverse separations on the order of a few kiloparsecs. However, small separation lenses are scarce and only a few such studies have been made.

Weymann & Foltz (1983) were the first to study the absorber sizes using common absorption lines in the quad lens PG 1115+080 ($\Delta\theta = 2''.2$, $z = 1.72$) finding a lower limit on the transverse dimension of 0.24 h_{100}^{-1} kpc. A subsequent study by Foltz et al. (1984) of Q2345+007 ($\Delta\theta = 7''.1$, $z = 2.15$), increased this limit to 2.5–12 h_{100}^{-1} kpc. Smette et al. (1992) found that the equivalent widths of common $\text{Ly}\alpha$ lines found in the pair UM 673 ($\Delta\theta = 2''.2$, $z = 2.72$) are highly correlated with no detected velocity variations; this work yields a lower bound on size derived for spherical clouds of 6 h_{100}^{-1} kpc. A study of the pair HE 1104–1805 ($\Delta\theta = 3''.0$, $z = 2.32$) by Smette et al. (1995) confirmed this

result and lead to a model-dependent lower limit to the characteristic size of the Ly α absorbers of $\sim 50 h_{100}^{-1}$ kpc. In apparent contradiction, Bechtold & Yee (1995) obtained ground-based spectra of two components of the quad lens B1422+231 ($\Delta\theta = 1''.3$, $z = 3.63$). They found that while the transverse separation is too small to provide useful size constraints on the absorbers, the equivalent widths were correlated but not identical, implying that the high-redshift Ly α absorbers are clumpy on scales of $0\text{--}0.15 h_{100}^{-1}$ kpc.

Nonlensed quasar pairs with larger separations ($\Delta\theta > 10''$) have traditionally been used to put upper limits on the transverse size of the hydrogen absorbers (Sargent, Young, & Schneider 1982; Shaver & Robertson 1983). More recently, coincident Ly α lines in quasar pairs have been used to define characteristic sizes for the hydrogen absorbers over a range of redshifts (Dinshaw et al. 1994, 1995, 1997; Bechtold et al. 1994). These large transverse sizes, $50\text{--}500 h_{100}^{-1}$ kpc, are difficult to understand in terms of traditional absorber models (i.e., Weymann, Carswell, & Smith 1981), but they have a ready explanation in the context of N -body simulations of large-scale structure which incorporate gas dynamics (Cen et al. 1994; Katz, Weinberg, & Hernquist 1996). The simulations indicate that the low column density hydrogen absorbers are filamentary structures of low overdensity which incorporate most of the baryons in the universe and are good tracers of the dark matter distribution.

The gravitationally lensed quasar B1422+231 provides an unprecedented probe of small-scale structure at high redshift. B1422+231 is an optically bright, flat-spectrum, radio-loud quasar discovered in a survey for small separation gravitational lenses by Patnaik et al. (1992), who resolved four components within a diameter of $1''.3$ and measured a redshift of 3.62. The image positions were subsequently confirmed in the infrared by Lawrence et al. (1992) and optically by Remy et al. (1993) and Yee & Ellingson (1994). Models of the lens system (Kormann, Schneider, & Bartelmann 1994; Hogg & Blandford 1994) are able to account for the positions and optical magnifications with a single elliptical galaxy as the primary deflector, with the possible addition of shear from galaxies to the southeast. Using ground-based spectra Hammer et al. (1995) measured a redshift of 0.647 based on a weak [O III] emission line for the lensing galaxy whose spectral properties are consistent with a late-type spiral. Impey et al. (1996) used *Hubble Space Telescope* (*HST*) imaging to reveal the lens at its predicted location near component D and found its photometric properties to be consistent with that of an elliptical at $z \sim 0.4$. Very recently, the redshift of the lensing galaxy was determined by two groups, each of whom used Keck LRIS spectra to obtain $z_{\text{lens}} = 0.3366$ (Tonry 1997) and $z_{\text{lens}} = 0.3374$ (Kundić et al. 1997).

This paper presents new spectroscopy obtained with *HST*'s Faint Object Spectrograph (FOS) for each of the four components of the B1422+231 system. The *HST* spectra of this object clearly show the system is a lens and a new redshift for the quasar is measured to be 3.6261. The analysis of three of the four lines of sight are consistent with no spatial inhomogeneities and no velocity variations on scales of $0\text{--}0.14 h_{100}^{-1}$ kpc at redshifts $2.9 \leq z \leq 3.5$. The structure of the paper is as follows: in § 2 the observations and reductions are described, in § 3.1 the line selection and measurement algorithm is summarized (details and an evaluation of the software using simulated data are present-

ed in the Appendix), in § 3.2 the metal line absorber identification process is described and the Ly α sample is defined, in § 3.3 comparisons of spectral properties are made between lines of sight using line-fitting dependent and independent methods, in § 4 the results are summarized, and a brief discussion of the implications for absorber size and geometry is presented in § 5. Throughout this paper an Einstein-DeSitter universe is assumed with $H_0 = 100 \text{ km s}^{-1} \text{ Mpc}^{-1}$.

2. OBSERVATIONS

Each of the four components of the quasar's lensed image were observed spectroscopically with *HST*'s FOS using the red Digicon detector and the $0''.26$ (diameter) circular aperture. Because the four components are separated by a maximum of only $1''.3$ and a minimum of $0''.51$, steps were taken to ensure that each of the images was centered properly in the aperture. This was achieved by "peaking up" on a nearby star, offsetting to the brightest component B, and imaging it with FOS using a mirror in place of a grating. Offsets using astrometric coordinates (Patnaik et al. 1992) were then made from component B to each of the other three components and subsequent imaging through FOS verified the coordinates and pointing were sufficient to place each source in the aperture. The four stage peak-up used has a centering accuracy of $\leq 0''.04$. The mirror was replaced with grating G570H, which gives a dispersion of $1.09 \text{ \AA pixel}^{-1}$ and a spectral resolution of 4.02 \AA FWHM (FOS Instrument Handbook v. 6.0). Spectra were obtained on 1995 March 27, at 15:08:46, 14:42:27, 16:30:49, and 18:14:54 UT with total exposure times of 1200, 1200, 2400, and 4800 s for components A–D, respectively. Spectral coverage is from 4569 to 6818 Å, which at the redshift of the quasar includes Ly α emission and a portion of the Ly α forest.

The data reduction was performed by STScI's "pipeline" using the recommended calibration files. Errors were calculated, a conversion was made to count rate, and the dark current was subtracted. No correction was made for scattered light but its contribution is estimated to be much less than the dark current; the dark current itself is much smaller ($< 1\%$) than the flux for any component at any wavelength. The data were flat-fielded using the recommended superflats, and wavelength and flux calibration were then performed. Any time dependent features in the superflats are small enough on instrumental resolution scales that residual features introduced by the flat-fielding procedure are not detectable within the errors in the flux measurement. Errors in the zero point of the wavelength scale obtained from the standard wavelength calibration are dominated by the nonrepeatability in the positioning of the filter-grating wheel and are of order 0.35 diodes or 1.5 Å; errors due to nonlinearity in the wavelength scale are very small compared to this. The dominant error in photometric calibration results from loss of signal due to inaccurate target centering, however, because of the peak-up process used to acquire the targets only about 3%–5% of the flux is thought to have been lost due to miscentering. Photometric calibration is estimated to be accurate to approximately 5%, which is more than sufficient for the purposes of this work.

The contamination in each spectrum by light from neighboring components may be estimated by considering the extent of the point spread function (PSF) whose flux falls to

zero at a radius of $0''.53$. Since the aperture radius is $0''.13$ components having separations of less than $0''.66$ will be contaminated by some amount of light from its neighbor. All of the components have separations exceeding this limit except for A and B ($\Delta\theta = 0''.51$); however, the region of overlap is on the tail of the PSF and the estimated upper limit on the fraction of the total light that is contributed to the spectrum of the neighboring component is $\sim 1\%$. More specifically, from the published F480LP magnitudes (Impey et al. 1996), the contamination of the A spectrum due to light from B is computed to be 1.3%, and the fraction of flux in the B spectrum due to A is 0.8%. The individual spectra are displayed in Figure 1. Photometry for each component as well as for the lensing galaxy has also been obtained, and the results and interpretation have been presented elsewhere (Impey et al. 1996).

3. ANALYSIS

3.1. Line Selection and Measurement

The measurement and interpretation of absorption lines is challenging at several levels. Line-profile fitting implicitly assumes that the regions causing the absorption are discrete structures in thermodynamic equilibrium that are well described by the chosen profile. However, supercomputer simulations have shown that instead of discrete clouds, the structure of the absorbing regions is filamentary and dis-

plays a wide variety of dynamical processes, each of which has an influence on the resultant spectral profile (Cen et al. 1994; Hernquist et al. 1996; Miralda-Escudé et al. 1996). At high redshift, the rapid increase in the number of weak lines makes deblending these overlapping profiles difficult at best. Also, an accurate estimate of the continuum is limited by the cumulative effect of the many weaker lines that act to depress the continuum.

The observational study of the Ly α forest has been revolutionized by the capabilities of the Keck Telescopes and the HIRES Spectrograph. Superb spectra of B1422+231 have been obtained by two groups (Songaila & Cowie 1996; Womble, Sargent, & Lyons 1996), although the spectra and line lists have not yet been published. In our case, we require the high spatial resolution of *HST* to completely isolate each of the components of the lens system. However, at the low spectral resolution of the FOS, *all* of the absorption features are blends of many (~ 2 – 5) individual components seen in the Keck spectra, and any details in the profiles are degraded to the instrumental profile, which is well approximated by a Gaussian. Line-profile fitting is only one way to characterize the absorbing material and to look for variations in its physical properties across the lines of sight. To check these assumptions we also use methods that do not rely on profile fitting, line deblending, and continuum fitting.

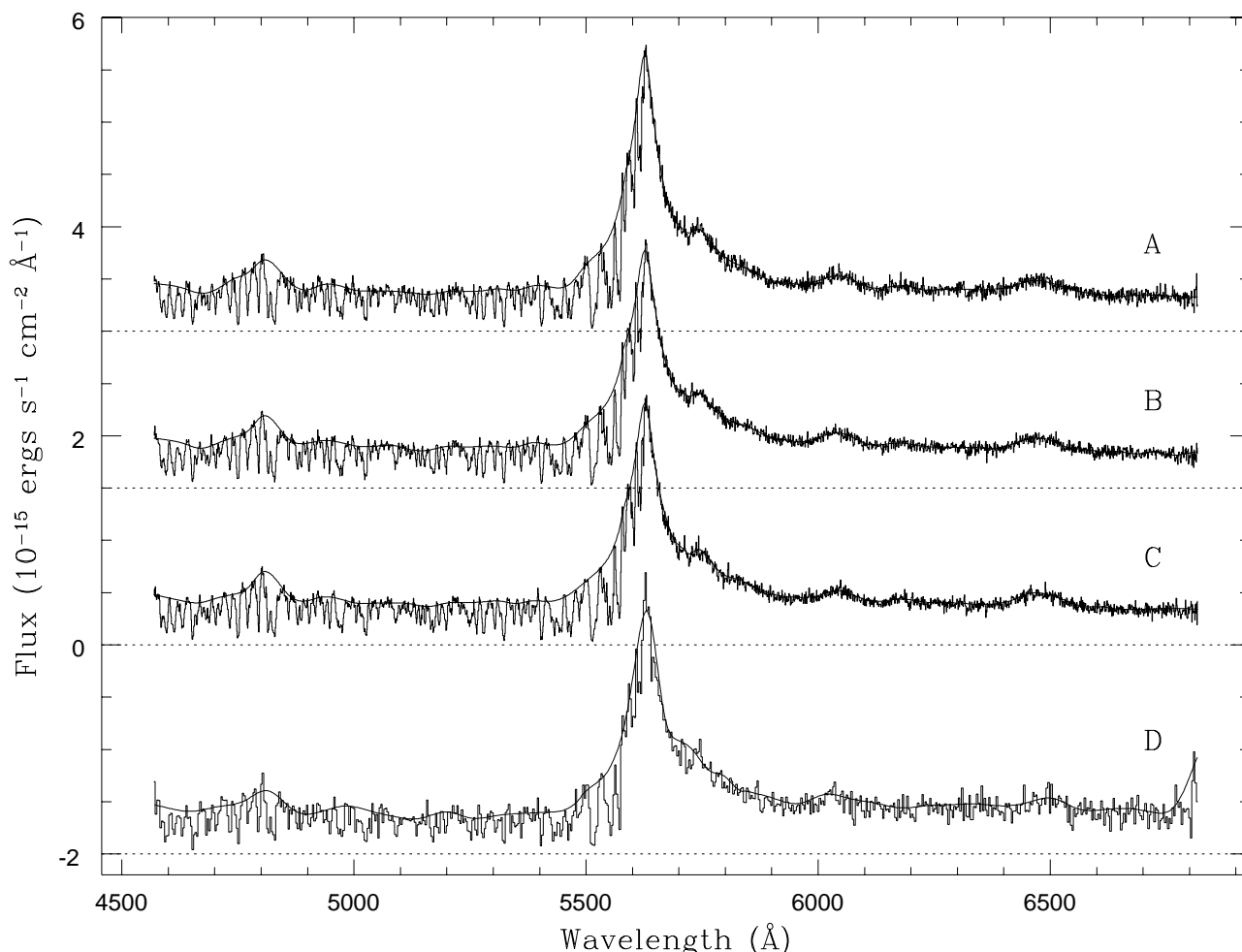


FIG. 1.—Spectra of the four components of B1422+231. The flux for component C is in units of 10^{-15} ergs s^{-1} cm^{-2} \AA^{-1} ; components A, B, and D have been scaled with respect to C using $\alpha_{AC} = 1.563$, $\alpha_{BC} = 2.014$, and $\alpha_{DC} = 0.051$ and are arbitrarily offset from C. The spectrum for component D has been smoothed by 3 pixels. The fitted continuum for each spectrum is overplotted.

3.1.1. Continuum Fitting

Software was developed based on code from Aldcroft (1993) to fit continua to the spectra and to select and measure absorption lines. Even though continuum fitting is generally difficult for high-redshift objects due to the high density of lines blueward of Ly α emission, we use a standard approach that is self-consistent and repeatable from component to component. A continuum was fitted to the spectrum of each component by dividing the spectrum into wide bins, whose size controls the tightness of the fit, and fitting the average of the points within each bin with a cubic spline. Any points deviating negatively from this fit by more than 2 times the error in the flux measurement at those points were flagged and eliminated from subsequent iterations of the fit. The bin size was set to be smaller near the wavelength of Ly α emission to follow the rapidly changing “continuum” over this region. This process was repeated four times, but the fit generally converged after two or three iterations. The final continuum fits are overplotted in Figure 1 for all four components.

The signal-to-noise ratio (SNR) for each spectrum was computed in two ways. The SNR per pixel (SNR_{pix}) was calculated because it was required to construct the simulated spectra used to evaluate the line-fitting software, and the SNR per resolution element (SNR_{res}) was computed to assess the data quality for comparison with other data sets. These two numbers were calculated for the section of the spectra to be used in the line-of-sight comparisons which is bounded by Ly β emission at the redshift of the quasar and Ly α emission less 6000 km s $^{-1}$, hereafter the “Ly α -only” region. At the redshift of the quasar, which is determined in § 3.1.2 of this paper to be $z_{\text{qso}} = 3.6261$, this region occupies a range in wavelength of 4745–5511 Å. The flat central portion (72%) of this region, 4900–5450 Å, was used in the SNR computations since the flux at both ends increases slightly and omitting them results in a lower bound for the measurement; the resulting SNR is broadly applicable to the entire spectrum. The SNR_{pix} is 14 ± 1 , 16 ± 1 , 24 ± 2 , and 4 ± 0.5 for components A–D, respectively. The SNR_{res} is 27 ± 4 , 32 ± 5 , 48 ± 7 , and 8 ± 1 for components A–D, respectively.

Because the parameters measured for the absorption lines will be compared in subsequent analyses, it is important to show that the fitted continua are not significantly different from one another. Component C has the highest SNR, so its spectrum is used as the reference. The ratios A/C, B/C, and D/C were formed and the rms of the residual in each pixel about the mean was computed. The ratio of the rms to the mean represents the level of difference between each pair of spectra and is 2.4%, 4.6%, and 16.7%, respectively. The only exception to this is the Ly α emission region of component A, which has a real difference in strength compared to the other lines of sight. This was discussed in the context of microlensing by Impey et al. (1996). The amount that any individual deviation could contribute to the measured equivalent width of an absorption line is smaller than the error in the equivalent width measurement itself, thus demonstrating that no discernible bias is introduced by fitting a separate continuum to each spectrum.

3.1.2. The QSO Redshift

All four spectra appear to be virtually identical and if the system is a lensed quasar, the redshifts of the four images should also be identical. The redshift of each of the four

components was measured using an IRAF routine that cross-correlates a template quasar spectrum with the data. Two templates were used: a composite of 48 high-redshift quasars (Hewett & Foltz 1997, private communication), and a composite of 718 quasars from the Large Bright Quasar Survey (LBQS) (Francis et al. 1991). The two independent measurements of the redshift made for each spectrum were combined in a weighted average to give redshifts of 3.6257 ± 0.0006 , 3.6264 ± 0.0007 , 3.6267 ± 0.0007 , and 3.6258 ± 0.0006 for A–D, respectively. There is a vanishing probability of finding four distinct quasars at the statistically identical redshifts within 1'3 on the sky, so this is unambiguous evidence supporting the lens nature of this system. Combining all eight independent measurements in a weighted average results in a redshift for the lensed quasar of 3.6261 with internal error of ± 0.0003 . The external error is dominated by the error in the zero point of the wavelength scale, which is 1.53 Å (*HST* FOS Instrument Handbook v. 6.0) or $\Delta z = 0.0002$ at Ly α emission. Adding the errors in quadrature gives a formal error of 0.0004. Note that although this precision is useful for intercomparing the redshifts of the four components, it may not reflect the accurate systemic redshift of the quasar due to the redshift dependence of the shape of the Ly α emission feature. This is because the composite spectra are predominantly composed of quasars at lower redshift so their Ly α emission lines are less eroded by Ly α forest absorption than that of B1422+231.

3.1.3. The Unresolved Line Profile

Hu et al. (1995) have found that the observed distribution of Doppler parameters derived from high-resolution, high SNR Keck spectra peaks around 25 km s $^{-1}$, which corresponds to a FWHM of 42 km s $^{-1}$. Fewer than 5% of the lines have FWHM of greater than ~ 100 km s $^{-1}$, so at the resolution of our FOS data (~ 170 –260 km s $^{-1}$), almost all of the lines will be unresolved. This is demonstrated by the spectra of this object taken with the Keck telescope (Songaila & Cowie 1996; Womble, Sargent, & Lyons 1996), where it can be seen that each feature in our data is made of ~ 5 features in the HIRES data. Because all lines are assumed to be unresolved and because of the high density of lines at the redshift of this quasar, $z = 3.6261$, we use the most accurate model of the instrumental line profile to deblend and measure the lines. The instrumental profile quoted by the FOS Instrument Handbook for a point source observed at 3400 Å is a Gaussian with a FWHM of 4.02 Å and is derived from computer models given the optical parameters of the telescope. Recently, the line spread function (LSF) was measured (Koratkar 1996) for post-COSTAR data with the 0'9 (1'0 pre-COSTAR) aperture. The LSF for the 0'26 (0'3 pre-COSTAR) aperture will not differ significantly from this as the dominant factor affecting the profile is the diode width. The best-fit Gaussian to the observed line profile has FWHM_{res} of 3.93 Å, which differs from the value derived from the models by $\sim 2\%$, and it was chosen as the best representation of the observed line profile.

3.1.4. Line-Profile Fitting

The procedure for locating and measuring line parameters is described in detail in the Appendix. The algorithm for selecting lines is based on that used in Paper II of the *HST* Quasar Absorption Line Key Project (Schneider et al. 1993). The Appendix summarizes the process for obtaining

a best fit of the unresolved line profile to the absorption features, and has a description of the subsequent derivation of line parameters. Finally, an evaluation of the software is made with three simple tests which use simulated data designed to characterize the FOS data.

There is no completely reliable way to recover line properties from blended and limited signal-to-noise data. However, the exhaustive procedure described in the Appendix (1) does not appear to underfit or overfit the spectra, (2) yields line parameters consistent with the noise, and (3) fits multiple lines in a blended region in a self-consistent way. The four spectra with the final fits overplotted are displayed in an expanded fashion in Figure 2, and the final line lists are presented in Tables 1, 2, 3, and 4. Note that the significance listed in the tables, SL, is calculated using the equivalent width error assigned by the deblending software, σ_W , and not σW_i or $\bar{\sigma} W_i$, which were used in the initial selection phase. As a result, there is no hard lower limit to the significances of lines listed in these tables, but significance limits are imposed for the inclusion of lines in further analyses.

3.2. Line Identification

3.2.1. Metal Lines

Our primary goal is to compare Ly α absorber properties between the four quasar lines of sight. However, the Ly α

forest suffers significant contamination from high-ionization metal lines associated primarily with strong C iv doublets identified redward of Ly α emission. Ideally, we would identify these metal lines individually in each spectrum and cull them from the list of potential Ly α lines. Note that in this situation we are concerned with strong metal line systems having hydrogen columns near the Lyman limit, not the ubiquitous but extremely weak metal lines that can be found as counterparts to most Ly α forest absorbers (Songaila & Cowie 1996). With sufficient resolution and signal-to-noise, metal lines can be identified purely by their small velocity widths; with FOS data we must resort to more indirect techniques.

Metal line systems for this quasar have been determined from searches for C iv doublets in higher resolution ground-based data (Bechtold & Yee 1995). One way to account for the presence of the metal lines in the Ly α forest is to calculate their effect statistically using the limiting equivalent width of each spectrum and a list of metal lines and strengths that are likely to be found in an absorption system. However, while such a list of likely lines exists (Morton, York, & Jenkins 1988), the estimated strengths are based on solar abundances. In practice, the equivalent widths of the Ly α lines predicted from the published equivalent widths for the C iv doublets differ from the observed equivalent widths of the Ly α lines by orders of magnitude.

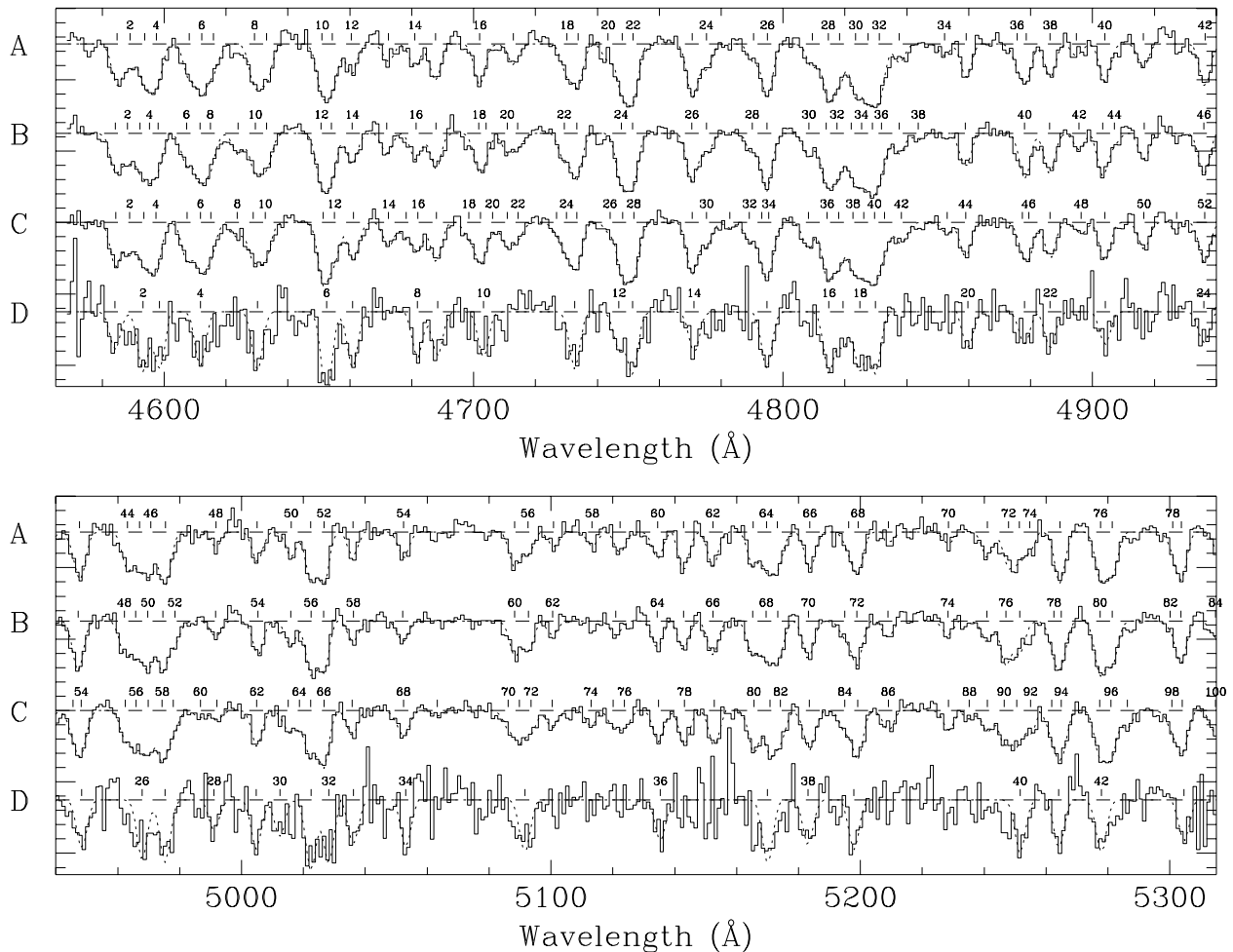


FIG. 2.—Spectra of the four components of B1422+231 normalized by their respective continua, offset arbitrarily from one another and expanded to show the details of the absorption features. The final fits to each absorption feature are overplotted in a dashed line but are often not distinguishable from the dark because of the goodness of the fit. The line centers are marked and numbered every other one.

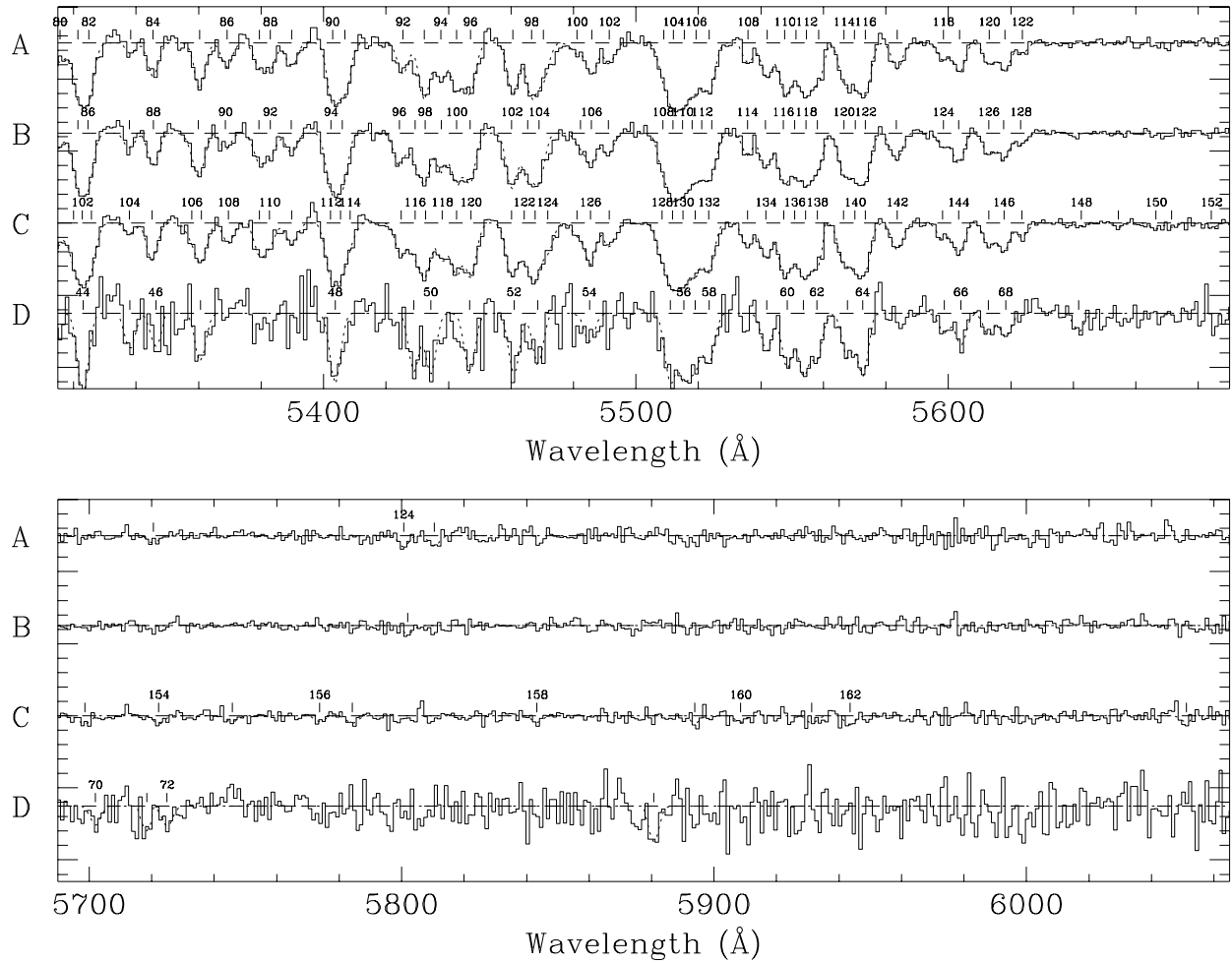


FIG. 2—Continued

Another possibility is to use the observed metal line ratios for 18 low-redshift, metal-rich quasars from Paper VI of the *HST* Quasar Absorption Line Key Project (Bergeron et al. 1994) to estimate the contamination rate of metal lines in the Ly α forest. Equivalent widths for 10 different species, most of which are doublets, are presented for 19 redshift systems in this sample of quasars. Unfortunately, the scatter in the ratio of equivalent widths of these lines for most combinations of species is too large for this technique to be effective.

A third option is to cross-correlate a template spectrum, which could be constructed to represent the transitions and strengths of lines typically found in a metal line absorption system, with the data to more accurately measure the known redshift systems and to define a narrow match region with which to identify additional member lines. This method also has the practical difficulty of defining “typical” strength ratios to be used in creating the template, and additionally, the Ly α forest is too blended to be able to distinguish peaks in the correlation function due to real absorption systems from those due to noise. However, it is possible to use the published metal line systems as a starting point to redetermine the redshifts of the absorption systems using the strongest transitions of the system, and a criteria may be developed for locating the additional associated metal lines. This is done for the spectrum of com-

ponent C, which has a SNR_{res} of almost 50, and the new redshifts are used to identify lines in all four components.

All seven metal systems found by Bechtold & Yee (1995) are confirmed by Womble et al. (1996) and so these redshifts were used to search for lines in a list of 40 strong absorption lines commonly found in quasars (Morton et al. 1988). The size of the match window was chosen to be $2.5\sigma_{\text{res}}$, which is small enough to minimize duplicate identifications in the crowded blueward region, and yet large enough to be able to pick out the weaker redward lines that have a larger uncertainty in central wavelength but are more sparsely distributed. The redshifts of the strongest identified lines, which could be any of Ly α , Ly β or components of doublets O vi $\lambda\lambda$ 1031/1037, Si iv $\lambda\lambda$ 1393/1402, and C iv $\lambda\lambda$ 1548/1550, were then averaged to redetermine the systemic redshift. The redetermined redshifts for each of the seven systems are as follows: 3.0806 ± 0.0017 , 3.3803 ± 0.0014 , 3.5121 ± 0.0008 , 3.5343 ± 0.0006 , 3.5375 ± 0.0011 , 3.5845 ± 0.0002 , and 3.6255 ± 0.0005 . These are also listed in Table 5 along with the number of lines used to evaluate each system and the previously published values. The systems at $z = 3.5343$ and $z = 3.5375$ are so close together that even though the Si iv and O vi doublets are identified for these systems only Ly α and Ly β , the very strongest of the lines, were used in calculating the redshift to avoid confusion by the weaker member candidates. However, if all six

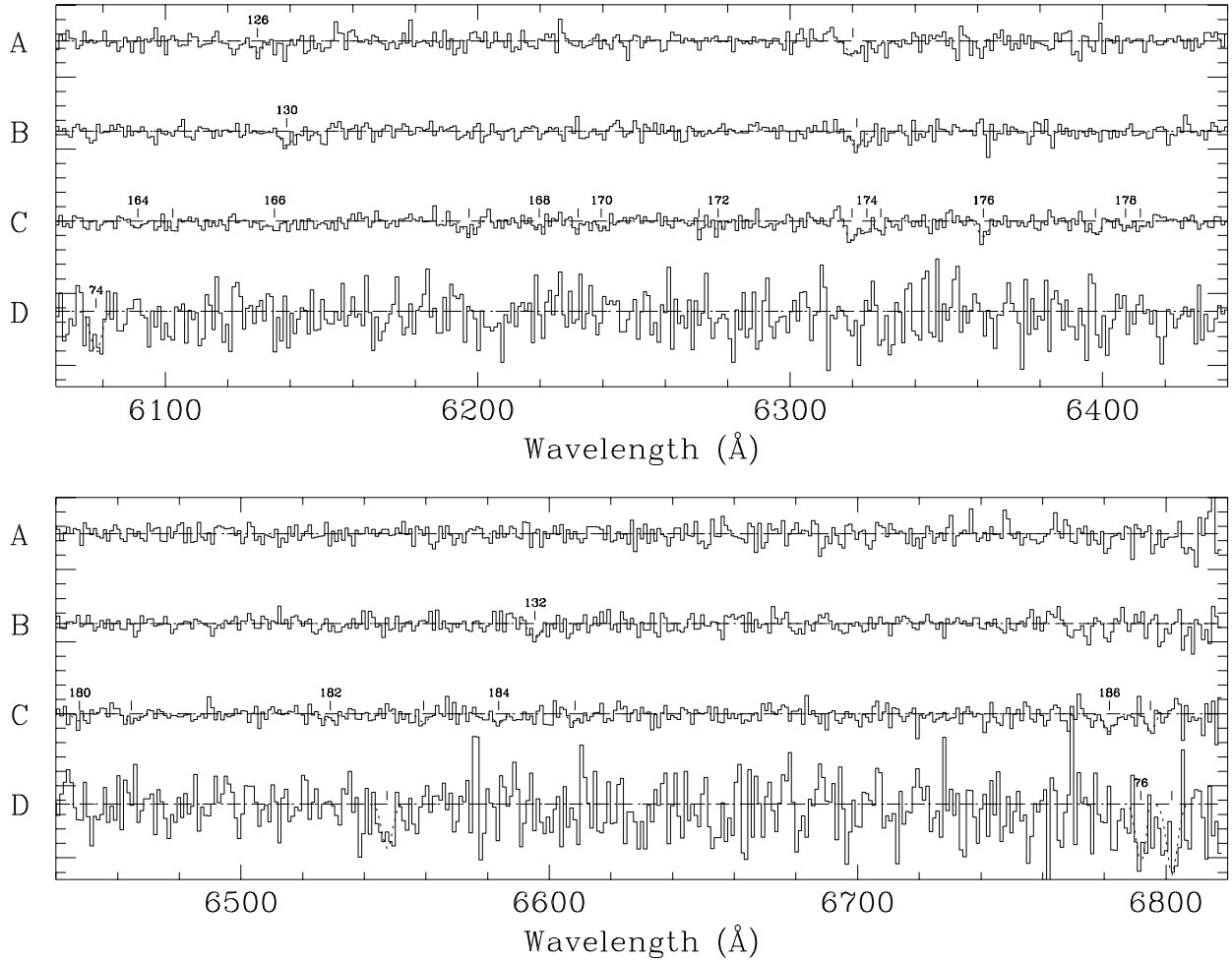


FIG. 2—Continued

strong lines identified with this system using the redshift obtained from the $\text{Ly}\alpha$ - β pair are used to obtain an average redshift, the result is identical to within the errors.

To identify new species in all seven metal line systems, a search was made for candidate identifications using the new redshift values, the Morton comparison line list, and the same match window. $\text{Ly}\alpha$ is required to be the strongest line in the system so candidate metal identifications are excluded if they have equivalent widths of greater than 90% of the equivalent width of $\text{Ly}\alpha$ for that system. In A, B, and C for all seven redshift systems the equivalent widths for $\text{Ly}\alpha$ are greater than for $\text{Ly}\beta$ except for in systems $z = 3.5343$ and $z = 3.5375$, where $\text{Ly}\alpha$ falls on the $\text{Ly}\alpha$ emission feature and the fitted continuum is less certain. To implement this criterion in these cases an equivalent width for $\text{Ly}\alpha$ is estimated from the $\text{Ly}\beta$ line using the strengths tabulated in Table 4 of Morton et al. (1988). For pairs of lines identified as a doublet, one component must be stronger or weaker than the other in the same sense as expected by the tabulated strengths in the Morton list unless it is doubly identified in the final line lists. If only the stronger component of a doublet is identified, the weaker component is required to have either an expected position falling in a blended region or a strength of less than 5σ for the stronger component to be accepted. If only the weaker component is identified, the expected position of the stronger component is required to lie in a blend and its expected strength must

not be greater than $\text{Ly}\alpha$ for the system. Two exceptions were made for very weak lines falling in the $\text{Ly}\alpha$ emission region where the continuum fit is less certain.

If after this process a line is doubly identified, the line that is both closer and stronger was taken to be the correct identification, otherwise the identification for the weaker line is indicated as a footnote in Tables 1–4, where all of the identifications are listed. Several lines for close systems $z = 3.5343$ and $z = 3.5375$ are not resolved in A and B but match within the specified range so they are both listed as double, and in two cases triple, identifications. For component D the SNR is so low that each metal line is blended with many $\text{Ly}\alpha$ lines and deblending them is not possible. This explains why for three out of five of the metal line systems where $\text{Ly}\alpha$ was identified, the line identified as $\text{Ly}\beta$ is stronger than that of $\text{Ly}\alpha$, and for two of the seven systems where $\text{Ly}\alpha$ was expected, none is identified. For this reason, only $\text{Ly}\alpha$ and $\text{Ly}\beta$ associated with each absorption system is listed for component D.

The total number of lines identified with each of the metal line absorption systems is 26, 28, 48, and 10, or 20%, 21%, 26%, and 13% of the total line lists for A–D, respectively. The total number of lines associated with the individual absorption systems for each component is presented in Table 5. The total number of identified lines that fall in the “ $\text{Ly}\alpha$ -only” region (4745–5511 Å) are 11, 9, 13, and 3 for A–D, respectively, which is 13%, 10%, 13%, and 7% of the

TABLE 1
LINE LIST FOR B1422+231: COMPONENT A

Line	λ_{vac} (Å)	Equivalent Width (Å)	SL ^a	χ^2_v	Redshift	Identification	Residual (Å)
1.....	4584.78 ± 0.18	2.45 ± 0.16	15.7	1.50
2.....	4588.93 ± 0.34	1.49 ± 0.16	9.3	1.50
3.....	4593.77 ± 0.21	2.44 ± 0.15	16.2	1.50
4.....	4597.44 ± 0.17	2.65 ± 0.15	17.1	1.50
5.....	4608.06 ± 0.22	2.02 ± 0.15	13.1	2.63
6.....	4612.12 ± 0.19	2.94 ± 0.14	21.5	2.63
7.....	4615.95 ± 0.29	1.65 ± 0.17	9.5	2.63
8.....	4629.25 ± 0.18	2.49 ± 0.16	16.0	2.63	3.5121	H I λ 1025	1.13
9.....	4633.06 ± 0.20	2.27 ± 0.16	14.2	2.63
10.....	4650.98 ± 0.18	2.81 ± 0.18	15.6	1.76	3.5343	H I λ 1025	0.04
11.....	4654.32 ± 0.19	2.62 ± 0.18	14.5	1.76	3.5375	H I λ 1025	0.14
12.....	4660.52 ± 0.20	1.86 ± 0.15	12.5	1.76
13.....	4672.46 ± 0.40	1.04 ± 0.16	6.3	1.49
14.....	4681.04 ± 0.31	1.39 ± 0.18	7.9	1.49	3.5121	O VI λ 1037	-0.74
15.....	4687.65 ± 0.18	2.20 ± 0.15	14.3	1.49
16.....	4701.97 ± 0.14	2.46 ± 0.13	19.7	1.00	3.5845	H I λ 1025	-0.42
17.....	4712.86 ± 0.30	1.22 ± 0.15	8.2	1.00
18.....	4730.15 ± 0.26	1.79 ± 0.16	10.9	1.65
19.....	4733.80 ± 0.18	2.42 ± 0.15	15.9	1.65
20.....	4743.48 ± 0.39	1.00 ± 0.15	6.6	2.60	3.6255	H I λ 1025	-1.01
21.....	4748.06 ± 0.16	2.88 ± 0.12	23.7	2.60
22.....	4751.54 ± 0.12	3.26 ± 0.12	26.2	2.60
23.....	4770.71 ± 0.10	3.16 ± 0.10	32.8	0.95
24.....	4775.25 ± 0.23	1.48 ± 0.13	11.5	0.95
25.....	4790.45 ± 0.33	1.02 ± 0.13	7.9	2.19
26.....	4794.96 ± 0.08	3.26 ± 0.09	36.6	2.19
27.....	4809.47 ± 0.21	1.42 ± 0.12	12.1	3.20
28.....	4814.57 ± 0.11	3.30 ± 0.10	33.1	3.20
29.....	4818.26 ± 0.17	2.22 ± 0.12	18.1	3.20
30.....	4823.50 ± 0.11	3.03 ± 0.10	30.8	3.20
31.....	4827.43 ± 0.12	3.20 ± 0.09	34.8	3.20
32.....	4831.07 ± 0.10	3.28 ± 0.10	33.1	3.20
33.....	4837.60 ± 0.27	1.13 ± 0.13	8.8	3.20
34.....	4852.19 ± 0.51	0.68 ± 0.14	4.8	0.78
35.....	4859.20 ± 0.17	1.98 ± 0.12	16.1	2.71
36.....	4875.61 ± 0.75	0.96 ± 0.33	2.9	0.83
37.....	4878.54 ± 0.32	2.16 ± 0.32	6.8	0.83
38.....	4886.29 ± 0.18	2.00 ± 0.14	14.7	0.83
39.....	4894.75 ± 0.58	0.70 ± 0.17	4.2	1.97	3.0806	N I λ 1200	-1.95
40.....	4904.00 ± 0.15	2.30 ± 0.13	17.6	1.25
41.....	4916.37 ± 0.27	1.35 ± 0.15	9.3	0.35	3.5343	N II λ 1083 ^b	1.22
42.....	4936.36 ± 0.12	2.51 ± 0.12	21.3	1.25
43.....	4947.69 ± 0.10	2.90 ± 0.11	26.9	2.32
44.....	4963.17 ± 0.22	2.16 ± 0.16	13.1	2.49	3.0806	H I λ 1215	2.53
45.....	4967.12 ± 0.35	2.00 ± 0.18	11.2	2.49
46.....	4970.68 ± 0.24	2.41 ± 0.19	13.0	2.49	3.5845	N II λ 1083	1.16
47.....	4975.41 ± 0.11	3.19 ± 0.11	28.7	2.49
48.....	4991.71 ± 0.44	0.90 ± 0.16	5.7	1.80
49.....	5005.09 ± 0.23	1.77 ± 0.16	11.0	1.10
50.....	5016.06 ± 0.32	1.48 ± 0.19	7.8	1.35
51.....	5022.41 ± 0.16	2.89 ± 0.16	18.4	1.35
52.....	5026.64 ± 0.14	2.99 ± 0.14	22.0	1.35
53.....	5035.98 ± 0.35	1.39 ± 0.19	7.4	2.12
54.....	5052.43 ± 0.27	1.55 ± 0.17	9.1	1.35
55.....	5088.22 ± 0.22	2.06 ± 0.16	13.1	0.82
56.....	5092.53 ± 0.36	1.34 ± 0.17	7.8	0.82
57.....	5100.84 ± 0.46	0.89 ± 0.17	5.4	1.58
58.....	5113.31 ± 0.49	0.84 ± 0.17	5.1	1.80
59.....	5122.30 ± 0.33	1.24 ± 0.16	7.7	1.41
60.....	5134.50 ± 0.25	1.57 ± 0.16	9.9	1.20
61.....	5142.88 ± 0.20	2.29 ± 0.18	12.8	2.07
62.....	5152.32 ± 0.25	2.02 ± 0.19	10.4	0.92
63.....	5165.28 ± 0.25	2.00 ± 0.17	12.1	1.16
64.....	5169.69 ± 0.33	2.12 ± 0.20	10.4	1.16
65.....	5173.18 ± 0.28	2.16 ± 0.22	9.8	1.16
66.....	5183.67 ± 0.17	2.19 ± 0.14	15.7	0.60
67.....	5196.15 ± 0.83	0.89 ± 0.32	2.8	1.53
68.....	5199.21 ± 0.29	2.35 ± 0.30	7.8	1.53
69.....	5209.09 ± 0.81	0.61 ± 0.18	3.4	2.63
70.....	5228.42 ± 0.60	0.70 ± 0.17	4.1	1.55
71.....	5241.04 ± 0.26	1.53 ± 0.15	9.9	2.88
72.....	5247.86 ± 0.35	1.94 ± 0.29	6.6	2.88

TABLE 1—*Continued*

Line	λ_{vac} (Å)	Equivalent Width (Å)	SL ^a	χ^2_{ν}	Redshift	Identification	Residual (Å)
73.....	5251.30 ± 0.72	1.51 ± 0.26	5.8	2.88
74.....	5254.76 ± 0.74	1.00 ± 0.31	3.2	2.88	3.3803	N I λ 1200	−1.65
75.....	5264.41 ± 0.11	3.02 ± 0.12	24.7	1.89
76.....	5277.59 ± 0.16	2.79 ± 0.15	18.9	1.23
77.....	5281.41 ± 0.18	2.56 ± 0.15	16.6	1.23
78.....	5300.88 ± 1.00	0.79 ± 0.36	2.2	1.30
79.....	5303.73 ± 0.27	2.68 ± 0.34	7.8	1.30
80.....	5315.67 ± 0.34	1.17 ± 0.16	7.3	1.04	3.0806	O I λ 1302	2.07
81.....	5321.44 ± 0.15	3.00 ± 0.15	20.6	1.04
82.....	5324.84 ± 0.14	3.19 ± 0.14	22.5	1.04	3.3803	H I λ 1215	−0.21
83.....	5338.26 ± 0.74	0.62 ± 0.18	3.5	1.12
84.....	5345.44 ± 0.19	1.94 ± 0.15	13.1	1.58
85.....	5360.36 ± 0.13	2.71 ± 0.13	21.7	0.82
86.....	5369.08 ± 0.27	1.41 ± 0.15	9.1	1.11	3.5121	Si II λ 1190	−2.15
87.....	5379.44 ± 0.42	1.40 ± 0.22	6.2	0.72
88.....	5382.98 ± 0.41	1.46 ± 0.22	6.6	0.72	3.5121	Si II λ 1193	−1.22
89.....	5389.79 ± 0.27	1.44 ± 0.15	9.3	0.72
90.....	5402.88 ± 0.09	3.54 ± 0.11	33.7	3.17
91.....	5406.82 ± 0.11	3.12 ± 0.12	26.5	3.17
92.....	5425.42 ± 0.20	1.87 ± 0.15	12.5	3.41
93.....	5432.22 ± 0.10	3.34 ± 0.11	29.6	3.41
94.....	5437.51 ± 0.17	2.30 ± 0.14	16.6	3.41
95.....	5442.66 ± 0.14	2.91 ± 0.13	22.9	3.41
96.....	5447.03 ± 0.13	2.95 ± 0.13	22.8	3.41
97.....	5460.64 ± 0.11	3.12 ± 0.12	25.2	1.60
98.....	5466.59 ± 0.14	3.16 ± 0.15	21.2	1.60
99.....	5470.40 ± 0.22	2.17 ± 0.17	12.5	1.60	3.5343	Si III λ 1206	−0.25
100.....	5481.12 ± 0.69	0.61 ± 0.16	3.8	1.60
101.....	5485.84 ± 0.21	1.89 ± 0.14	14.0	1.60	3.5121	H I λ 1215	0.66
102.....	5491.46 ± 0.28	1.22 ± 0.14	9.0	1.60
103.....	5508.93 ± 0.26	1.94 ± 0.22	8.9	1.58
104.....	5512.05 ± 0.20	3.27 ± 0.14	23.9	1.58	3.5343	H I λ 1215	−0.18
105.....	5515.48 ± 0.16	3.21 ± 0.11	28.6	1.58	3.5375	H I λ 1215	−0.59
106.....	5519.25 ± 0.16	2.74 ± 0.12	23.4	1.58	3.3803	Si II λ 1260	−1.83
107.....	5523.50 ± 0.11	2.95 ± 0.10	29.1	1.58
108.....	5535.90 ± 0.26	1.18 ± 0.12	10.0	2.44
109.....	5542.03 ± 0.13	2.14 ± 0.10	20.9	2.44
110.....	5547.65 ± 0.14	2.93 ± 0.14	20.5	2.44
111.....	5551.20 ± 0.38	1.70 ± 0.16	10.8	2.44
112.....	5554.62 ± 0.21	2.87 ± 0.14	20.2	2.44
113.....	5558.44 ± 0.18	2.19 ± 0.14	15.8	2.44
114.....	5566.62 ± 0.22	2.13 ± 0.20	10.8	2.73
115.....	5569.91 ± 0.30	2.11 ± 0.16	13.3	2.73
116.....	5573.47 ± 0.12	2.95 ± 0.14	21.6	2.73	3.5845	H I λ 1215	0.27
117.....	5583.64 ± 0.13	1.54 ± 0.08	18.5	2.98
118.....	5598.41 ± 0.21	1.04 ± 0.08	12.4	0.90
119.....	5603.52 ± 0.11	1.74 ± 0.07	23.5	0.90
120.....	5613.11 ± 0.14	1.33 ± 0.07	18.7	1.71
121.....	5618.07 ± 0.11	1.69 ± 0.07	25.5	1.71
122.....	5623.64 ± 0.29	0.64 ± 0.07	8.9	1.71	3.6255	H I λ 1215	0.55
123.....	5720.51 ± 0.68	0.43 ± 0.13	3.5	0.48	3.5375	Si II λ 1260	1.38
124.....	5800.64 ± 0.54	0.66 ± 0.14	4.6	0.82
125.....	5810.40 ± 0.59	0.60 ± 0.15	4.1	1.37
126.....	6129.53 ± 0.74	0.69 ± 0.20	3.4	0.54
127.....	6320.15 ± 0.61	0.94 ± 0.24	3.8	1.24	3.0806	C IV λ 1548 ^c	2.59

^a Significance of the line defined as W/σ_W .^b Also identified at $z = 3.5375$ as N II λ 1083 with residual -2.20 Å.^c Also identified at $z = 3.5343$ as Si IV λ 1393 with residual 0.43 Å.

total number of lines found in this region. Where there are coincidences of metal lines across lines of sight, the lines are identically identified. Coincidences and anticoincidences across lines of sight for the metal lines are discussed further in § 3.3.1.

An attempt was made to locate metal lines associated with the lensing galaxy. A redshift for the lensing galaxy has been measured by Tonry (1997) to be $z_{\text{lens}} = 0.3366$, and Kundić et al. (1997) obtain $z_{\text{lens}} = 0.3374$. The average of these measurements, $z_{\text{lens}} = 0.3369$, is used in the subsequent search for metal lines and in the calculation of the

proper transverse separation between the lines of sight. Ca I λ 4227 and the Ca II λ 3933/3968 doublet are the only strong lines predicted to fall within the wavelength range of the four lines of sight. In the spectrum of C, line 149 is identified as Ca I λ 4227; the limiting equivalent width is too high to be able to detect this line as a significant feature in the other lines of sight. The following lines in each spectrum coincide with the Ca II doublet within $2.5\sigma_{\text{res}}$: A, lines 75 and 79; B, lines 78 and 83; C, lines 93 and 99; D, lines 41 and 43. However, the relative strengths of the lines are not as expected in all cases except A. This is most likely due to

TABLE 2
LINE LIST FOR B1422+231: COMPONENT B

Line	λ_{vac} (Å)	Equivalent Width (Å)	SL ^a	χ^2_{ν}	Redshift	Identification	Residual (Å)
1.....	4584.26 ± 0.20	2.32 ± 0.16	14.4	1.22
2.....	4588.15 ± 0.40	1.67 ± 0.16	10.2	1.22
3.....	4592.23 ± 0.56	1.97 ± 0.38	5.2	1.22
4.....	4595.29 ± 0.74	2.16 ± 0.29	7.5	1.22
5.....	4598.08 ± 0.48	1.74 ± 0.50	3.5	1.22
6.....	4607.23 ± 0.20	1.89 ± 0.13	14.4	1.98
7.....	4611.53 ± 0.20	2.73 ± 0.16	17.4	1.98
8.....	4614.89 ± 0.24	1.96 ± 0.19	10.5	1.98
9.....	4623.86 ± 0.26	1.28 ± 0.13	9.8	1.98
10.....	4629.41 ± 0.19	2.26 ± 0.15	15.6	1.98	3.5121	H I λ 1025	1.29
11.....	4633.10 ± 0.21	2.03 ± 0.15	13.4	1.98
12.....	4650.75 ± 0.15	2.86 ± 0.16	18.1	0.78	3.5343	H I λ 1025	-0.19
13.....	4653.99 ± 0.16	2.69 ± 0.16	16.7	0.78	3.5375	H I λ 1025	-0.19
14.....	4660.79 ± 0.17	1.88 ± 0.13	14.9	0.78
15.....	4671.93 ± 0.29	1.20 ± 0.14	8.8	1.86
16.....	4681.35 ± 0.23	1.62 ± 0.15	11.1	1.86	3.5375	O VI λ 1031 ^{b,c}	-0.99
17.....	4687.85 ± 0.16	2.10 ± 0.13	15.6	1.86
18.....	4701.70 ± 0.50	2.00 ± 0.65	3.1	2.40	3.5845	H I λ 1025 ^{d,e}	-0.69
19.....	4703.97 ± 1.12	0.87 ± 0.66	1.3	2.40	3.5343	O VI λ 1037	-0.90
20.....	4710.88 ± 0.50	1.10 ± 0.21	5.2	2.40	3.5375	O VI λ 1037	2.73
21.....	4714.28 ± 0.65	0.82 ± 0.22	3.8	2.40
22.....	4729.26 ± 0.23	1.60 ± 0.13	12.0	2.07
23.....	4733.31 ± 0.12	2.72 ± 0.11	24.0	2.07
24.....	4747.74 ± 0.11	2.97 ± 0.10	28.9	2.54
25.....	4751.40 ± 0.10	3.11 ± 0.10	31.7	2.54
26.....	4770.55 ± 0.10	2.90 ± 0.09	31.8	1.71
27.....	4775.23 ± 0.23	1.30 ± 0.12	11.1	1.71
28.....	4790.04 ± 0.23	1.21 ± 0.11	11.1	1.75
29.....	4794.77 ± 0.07	3.39 ± 0.07	48.2	1.75
30.....	4808.34 ± 0.18	1.43 ± 0.10	14.3	1.17
31.....	4813.90 ± 0.12	2.91 ± 0.11	25.8	1.17
32.....	4817.41 ± 0.15	2.62 ± 0.11	23.9	1.17
33.....	4822.08 ± 0.24	2.24 ± 0.19	11.6	1.17
34.....	4825.32 ± 0.28	2.65 ± 0.15	17.7	1.17
35.....	4828.82 ± 0.27	3.08 ± 0.16	19.5	1.17
36.....	4831.77 ± 0.29	1.96 ± 0.26	7.5	1.17
37.....	4837.57 ± 0.24	1.23 ± 0.11	11.0	1.17
38.....	4843.70 ± 0.83	0.38 ± 0.13	3.0	1.17
39.....	4858.96 ± 0.14	2.00 ± 0.11	18.1	3.70
40.....	4878.08 ± 0.10	2.73 ± 0.10	26.8	3.58
41.....	4886.14 ± 0.12	2.40 ± 0.11	21.9	3.58
42.....	4895.66 ± 0.35	0.98 ± 0.14	7.2	0.67	3.0806	N I λ 1200	-1.04
43.....	4903.31 ± 0.17	2.48 ± 0.15	17.0	2.31
44.....	4907.10 ± 0.79	0.59 ± 0.17	3.4	2.31
45.....	4916.67 ± 0.20	1.57 ± 0.12	13.1	3.05	3.5343	N II λ 1083 ^f	1.52
46.....	4936.02 ± 0.11	2.48 ± 0.10	24.1	1.64
47.....	4947.20 ± 0.09	3.01 ± 0.09	33.1	2.32
48.....	4962.12 ± 0.25	1.79 ± 0.17	10.7	1.58	3.0806	H I λ 1215	1.48
49.....	4965.86 ± 0.31	1.92 ± 0.15	12.8	1.58
50.....	4969.77 ± 0.16	2.80 ± 0.12	22.5	1.58
51.....	4974.55 ± 0.15	2.92 ± 0.12	24.9	1.58
52.....	4978.46 ± 0.34	1.27 ± 0.15	8.4	1.58
53.....	4991.67 ± 0.37	0.93 ± 0.14	6.7	0.59
54.....	5005.32 ± 0.17	2.00 ± 0.13	15.0	1.58
55.....	5015.89 ± 0.27	1.50 ± 0.16	9.2	1.58
56.....	5022.45 ± 0.13	3.10 ± 0.13	24.1	1.58
57.....	5026.56 ± 0.13	2.93 ± 0.12	24.6	1.58
58.....	5036.13 ± 0.34	1.19 ± 0.17	7.1	0.81
59.....	5052.13 ± 0.30	1.25 ± 0.15	8.2	0.41
60.....	5088.31 ± 0.18	2.05 ± 0.13	16.0	2.37
61.....	5092.67 ± 0.22	1.76 ± 0.13	13.1	2.37
62.....	5100.48 ± 0.44	0.83 ± 0.14	5.8	2.54
63.....	5120.97 ± 0.46	0.81 ± 0.15	5.4	1.49
64.....	5134.41 ± 0.22	1.58 ± 0.14	11.5	1.05
65.....	5142.80 ± 0.25	1.68 ± 0.17	9.7	0.46
66.....	5152.32 ± 0.21	1.99 ± 0.17	11.6	0.92
67.....	5165.21 ± 0.20	2.05 ± 0.14	14.5	1.11
68.....	5169.59 ± 0.24	2.23 ± 0.15	14.8	1.11
69.....	5173.34 ± 0.19	2.37 ± 0.16	15.1	1.11
70.....	5183.18 ± 0.14	2.22 ± 0.12	18.4	1.36
71.....	5194.93 ± 0.49	0.92 ± 0.17	5.4	2.13

TABLE 2—Continued

Line	λ_{vac} (Å)	Equivalent Width (Å)	SL ^a	χ^2_{ν}	Redshift	Identification	Residual (Å)
72.....	5198.87 ± 0.16	2.60 ± 0.14	18.7	2.13
73.....	5208.85 ± 0.38	0.93 ± 0.14	6.5	0.94
74.....	5228.27 ± 0.47	0.80 ± 0.15	5.5	1.83
75.....	5240.91 ± 0.29	1.20 ± 0.14	8.6	3.02
76.....	5247.00 ± 0.14	2.59 ± 0.12	20.9	3.02
77.....	5251.48 ± 0.19	1.93 ± 0.14	13.9	3.02
78.....	5262.55 ± 0.61	1.48 ± 0.56	2.6	3.02
79.....	5264.91 ± 0.41	2.20 ± 0.56	4.0	3.02
80.....	5277.41 ± 0.11	3.05 ± 0.11	26.8	1.75
81.....	5281.39 ± 0.15	2.55 ± 0.12	20.4	1.75
82.....	5300.13 ± 1.80	0.31 ± 0.22	1.4	0.84
83.....	5303.60 ± 0.21	2.45 ± 0.19	12.9	0.84
84.....	5314.79 ± 0.37	0.96 ± 0.15	6.6	0.83	3.0806	O I λ 1302	1.19
85.....	5321.39 ± 0.15	2.91 ± 0.15	19.8	0.83
86.....	5324.63 ± 0.14	2.99 ± 0.15	20.6	0.83	3.3803	H I λ 1215	−0.42
87.....	5337.89 ± 0.43	0.89 ± 0.15	6.1	2.30
88.....	5345.52 ± 0.17	1.93 ± 0.13	14.9	0.56
89.....	5359.96 ± 0.11	2.71 ± 0.11	24.5	1.54
90.....	5368.65 ± 0.36	0.94 ± 0.15	6.5	2.22	3.5121	Si II λ 1190	−2.58
91.....	5379.38 ± 0.29	1.68 ± 0.19	9.1	1.26
92.....	5382.95 ± 0.38	1.33 ± 0.19	7.1	1.26	3.5121	Si II λ 1193	−1.25
93.....	5389.70 ± 0.29	1.19 ± 0.14	8.6	1.26
94.....	5402.44 ± 0.11	3.23 ± 0.11	28.3	3.94
95.....	5406.04 ± 0.11	3.07 ± 0.12	26.0	3.94
96.....	5424.24 ± 0.19	1.95 ± 0.13	14.5	2.01
97.....	5429.32 ± 0.43	1.49 ± 0.23	6.4	2.01
98.....	5432.51 ± 0.22	2.70 ± 0.22	12.3	2.01
99.....	5437.71 ± 0.17	2.23 ± 0.13	17.4	2.01
100.....	5442.61 ± 0.12	2.94 ± 0.11	26.4	2.01
101.....	5446.95 ± 0.11	2.89 ± 0.11	25.3	2.01
102.....	5460.24 ± 0.09	3.29 ± 0.11	31.1	4.11
103.....	5465.34 ± 0.17	2.62 ± 0.15	18.0	4.11
104.....	5469.04 ± 0.15	2.83 ± 0.14	20.2	4.11	3.5343	Si III λ 1206	−1.61
105.....	5482.20 ± 0.64	0.78 ± 0.19	4.2	0.49
106.....	5485.73 ± 0.27	1.81 ± 0.17	10.5	0.49	3.5121	H I λ 1215	0.55
107.....	5491.12 ± 0.25	1.27 ± 0.12	10.5	0.49
108.....	5508.67 ± 0.27	1.98 ± 0.24	8.2	1.22
109.....	5511.79 ± 0.30	3.15 ± 0.17	18.3	1.22	3.5343	H I λ 1215	−0.44
110.....	5514.95 ± 0.45	2.80 ± 0.24	11.7	1.22	3.5375	H I λ 1215	−1.12
111.....	5517.97 ± 0.64	2.20 ± 0.25	8.7	1.22
112.....	5521.11 ± 0.60	2.01 ± 0.26	7.7	1.22	3.3803	Si II λ 1260	0.03
113.....	5524.21 ± 0.26	2.22 ± 0.29	7.6	1.22
114.....	5535.69 ± 0.21	1.28 ± 0.11	12.1	2.04
115.....	5541.49 ± 0.12	2.13 ± 0.09	23.1	2.04
116.....	5547.16 ± 0.12	2.83 ± 0.12	24.0	2.04
117.....	5550.81 ± 0.23	2.18 ± 0.12	18.2	2.04
118.....	5554.49 ± 0.18	2.77 ± 0.11	25.6	2.04
119.....	5558.10 ± 0.18	2.10 ± 0.14	15.5	2.04
120.....	5566.54 ± 0.16	2.34 ± 0.13	17.5	2.04
121.....	5570.18 ± 0.24	2.27 ± 0.13	17.5	2.04
122.....	5573.47 ± 0.15	2.60 ± 0.15	17.0	2.04	3.5845	H I λ 1215	0.27
123.....	5583.30 ± 0.12	1.62 ± 0.07	21.8	2.51
124.....	5598.41 ± 0.26	0.83 ± 0.08	10.2	2.03
125.....	5603.26 ± 0.11	1.79 ± 0.07	25.3	2.03
126.....	5612.93 ± 0.14	1.31 ± 0.07	19.1	0.89
127.....	5617.74 ± 0.12	1.58 ± 0.06	24.5	0.89
128.....	5623.19 ± 0.24	0.70 ± 0.07	10.3	0.89	3.6255	H I λ 1215	0.10
129.....	5801.96 ± 0.74	0.47 ± 0.13	3.5	1.49
130.....	6138.85 ± 0.49	0.87 ± 0.17	5.0	1.14
131.....	6321.28 ± 0.51	1.03 ± 0.21	4.8	1.39	3.5343	Si IV λ 1393 ^g	1.56
132.....	6595.39 ± 0.64	0.86 ± 0.23	3.8	0.58

^a Significance of the line defined as W/σ_W .^b Also identified at $z = 3.5121$ as O VI λ 1037 with residual -0.43 Å.^c Also identified at $z = 3.5343$ as O VI λ 1031 with residual 2.27 Å.^d Also identified at $z = 3.5343$ as C II λ 1036 with residual 2.63 Å.^e Also identified at $z = 3.5375$ as C II λ 1036 with residual -0.65 Å.^f Also identified at $z = 3.5375$ as N II λ 1038 with residual -1.90 Å.^g Also identified at $z = 3.5375$ as Si IV λ 1393 with residual -2.84 Å.

TABLE 3
LINE LIST FOR B1422+231: COMPONENT C

Line	λ_{vac} (Å)	Equivalent Width (Å)	SL ^a	χ^2_{ν}	Redshift	Identification	Residual (Å)
1.....	4584.31 ± 0.09	2.58 ± 0.08	33.5	2.80
2.....	4588.84 ± 0.14	1.87 ± 0.08	22.5	2.80
3.....	4593.44 ± 0.11	2.54 ± 0.08	32.9	2.80
4.....	4597.32 ± 0.08	2.93 ± 0.07	39.3	2.80
5.....	4607.43 ± 0.10	2.29 ± 0.08	27.9	4.56
6.....	4611.75 ± 0.13	2.74 ± 0.11	25.9	4.56
7.....	4615.09 ± 0.17	1.89 ± 0.13	14.7	4.56
8.....	4623.64 ± 0.26	0.90 ± 0.09	9.8	4.56
9.....	4628.82 ± 0.13	2.21 ± 0.09	24.4	4.56	3.5121	H I λ 1025	0.70
10.....	4632.63 ± 0.12	2.30 ± 0.09	25.0	4.56
11.....	4651.40 ± 0.06	3.52 ± 0.07	47.0	3.61	3.5343	H I λ 1025	0.46
12.....	4654.98 ± 0.12	2.26 ± 0.09	24.9	3.61	3.5375	H I λ 1025	0.80
13.....	4661.18 ± 0.09	2.33 ± 0.08	30.2	3.61
14.....	4672.54 ± 0.16	1.42 ± 0.09	16.1	3.56
15.....	4678.17 ± 0.40	0.85 ± 0.12	7.1	3.56	3.5343	O VI λ 1031	-0.91
16.....	4682.05 ± 0.19	1.73 ± 0.11	15.2	3.56	3.5375	O VI λ 1031	-0.29
17.....	4687.94 ± 0.10	2.35 ± 0.09	26.6	3.56
18.....	4698.40 ± 0.40	0.85 ± 0.13	6.7	2.81	3.5343	C II λ 1036	-0.67
19.....	4702.25 ± 0.17	2.47 ± 0.10	24.7	2.81	3.5845	H I λ 1025 ^b	-0.14
20.....	4706.11 ± 0.87	0.47 ± 0.12	3.9	2.81	3.5343	O VI λ 1037 ^c	1.24
21.....	4710.87 ± 0.31	1.38 ± 0.13	10.8	2.81
22.....	4714.31 ± 0.37	0.92 ± 0.15	6.3	2.81
23.....	4726.84 ± 0.82	0.53 ± 0.19	2.8	0.86
24.....	4730.06 ± 0.38	1.66 ± 0.14	11.5	0.86
25.....	4733.37 ± 0.14	2.58 ± 0.15	17.2	0.86
26.....	4744.10 ± 0.41	0.63 ± 0.10	6.6	2.07	3.6255	H I λ 1025	-0.39
27.....	4748.21 ± 0.09	3.13 ± 0.07	44.2	2.07
28.....	4751.77 ± 0.08	3.05 ± 0.08	39.7	2.07
29.....	4770.62 ± 0.06	3.05 ± 0.06	52.9	2.05
30.....	4775.28 ± 0.14	1.46 ± 0.08	19.4	2.05
31.....	4782.82 ± 0.61	0.32 ± 0.08	4.1	1.89
32.....	4789.13 ± 0.26	1.08 ± 0.10	10.6	1.89
33.....	4793.16 ± 0.44	1.52 ± 0.32	4.7	1.89
34.....	4795.43 ± 0.20	2.64 ± 0.37	7.1	1.89
35.....	4808.15 ± 0.10	1.62 ± 0.06	25.7	4.48
36.....	4814.25 ± 0.06	3.23 ± 0.05	58.7	4.48
37.....	4817.98 ± 0.09	2.53 ± 0.06	39.9	4.48
38.....	4822.60 ± 0.12	2.62 ± 0.09	28.7	4.48
39.....	4826.05 ± 0.14	2.75 ± 0.08	34.1	4.48
40.....	4829.57 ± 0.13	3.22 ± 0.08	38.5	4.48
41.....	4832.85 ± 0.22	1.51 ± 0.12	12.1	4.48
42.....	4838.23 ± 0.15	1.28 ± 0.07	17.1	4.48
43.....	4852.96 ± 0.33	0.63 ± 0.08	7.7	3.43
44.....	4858.98 ± 0.09	2.04 ± 0.07	29.8	3.43
45.....	4877.34 ± 0.65	1.11 ± 0.57	2.0	4.14
46.....	4879.39 ± 0.44	1.69 ± 0.57	3.0	4.14
47.....	4886.33 ± 0.09	2.12 ± 0.08	28.0	4.14
48.....	4896.32 ± 0.32	0.68 ± 0.09	7.4	1.14	3.0806	N I λ 1200	-0.38
49.....	4904.00 ± 0.08	2.32 ± 0.07	32.8	4.00
50.....	4916.64 ± 0.13	1.58 ± 0.08	20.1	4.45	3.5343	N II λ 1083 ^d	1.49
51.....	4927.13 ± 0.59	0.38 ± 0.09	4.3	3.34
52.....	4936.23 ± 0.07	2.39 ± 0.07	34.0	3.88
53.....	4945.60 ± 0.37	1.20 ± 0.23	5.2	3.88
54.....	4948.25 ± 0.18	2.39 ± 0.23	10.4	3.88
55.....	4962.43 ± 0.20	1.63 ± 0.13	12.5	2.42	3.0806	H I λ 1215	1.79
56.....	4965.95 ± 0.22	2.01 ± 0.11	18.8	2.42
57.....	4969.81 ± 0.13	2.58 ± 0.09	27.4	2.42
58.....	4974.36 ± 0.12	2.89 ± 0.10	28.9	2.42
59.....	4977.90 ± 0.26	1.27 ± 0.13	10.0	2.42
60.....	4986.68 ± 0.59	0.42 ± 0.10	4.3	1.08
61.....	4992.00 ± 0.43	0.58 ± 0.09	6.2	1.08
62.....	5004.94 ± 0.11	2.12 ± 0.09	24.1	3.77
63.....	5015.03 ± 0.37	1.17 ± 0.18	6.6	4.67
64.....	5018.67 ± 0.75	0.85 ± 0.16	5.3	4.67
65.....	5022.40 ± 0.16	2.70 ± 0.12	22.0	4.67
66.....	5026.64 ± 0.08	3.28 ± 0.08	39.5	4.67
67.....	5035.82 ± 0.18	1.48 ± 0.11	13.8	4.27
68.....	5052.35 ± 0.14	1.63 ± 0.09	17.5	1.53
69.....	5063.28 ± 0.72	0.32 ± 0.10	3.3	0.69
70.....	5086.23 ± 0.38	0.98 ± 0.15	6.6	3.55
71.....	5089.76 ± 0.28	1.77 ± 0.12	14.2	3.55
72.....	5093.57 ± 0.26	1.28 ± 0.13	10.2	3.55

TABLE 3—*Continued*

Line	λ_{vac} (Å)	Equivalent Width (Å)	SL ^a	χ^2_{ν}	Redshift	Identification	Residual (Å)
73.....	5100.40 ± 0.22	1.05 ± 0.09	11.5	3.55
74.....	5112.91 ± 0.26	0.92 ± 0.09	9.8	2.88
75.....	5120.16 ± 0.38	0.91 ± 0.13	6.8	2.61
76.....	5123.76 ± 0.32	1.07 ± 0.13	8.0	2.61
77.....	5134.72 ± 0.11	1.85 ± 0.08	23.1	2.62
78.....	5143.14 ± 0.13	2.07 ± 0.11	19.4	2.62
79.....	5152.76 ± 0.14	2.08 ± 0.11	18.4	3.90
80.....	5165.60 ± 0.09	2.52 ± 0.08	32.2	3.11
81.....	5170.75 ± 0.14	2.53 ± 0.12	21.9	3.11
82.....	5174.18 ± 0.20	1.70 ± 0.13	13.3	3.11
83.....	5183.46 ± 0.08	2.35 ± 0.08	29.8	3.69
84.....	5194.99 ± 0.22	1.24 ± 0.10	12.5	3.59
85.....	5199.14 ± 0.08	2.86 ± 0.08	35.2	3.59
86.....	5209.00 ± 0.19	1.18 ± 0.09	12.6	5.46
87.....	5228.49 ± 0.18	1.20 ± 0.09	13.6	4.02
88.....	5235.20 ± 0.52	0.48 ± 0.10	4.8	4.02
89.....	5241.03 ± 0.20	1.26 ± 0.09	13.5	4.02
90.....	5246.41 ± 0.16	1.92 ± 0.10	19.1	4.02
91.....	5250.45 ± 0.16	2.08 ± 0.10	21.6	4.02
92.....	5254.94 ± 0.20	1.38 ± 0.10	13.7	4.02	3.3803	N I λ 1200	−1.47
93.....	5261.89 ± 0.28	1.41 ± 0.16	8.6	4.40
94.....	5264.93 ± 0.14	2.62 ± 0.15	17.0	4.40
95.....	5277.37 ± 0.10	2.65 ± 0.09	30.4	2.60
96.....	5281.01 ± 0.10	2.75 ± 0.09	32.0	2.60
97.....	5286.20 ± 0.23	1.06 ± 0.10	11.1	2.60	3.3803	Si III λ 1206	1.32
98.....	5300.66 ± 0.33	1.07 ± 0.14	7.7	2.82
99.....	5304.04 ± 0.14	2.48 ± 0.13	19.7	2.82
100.....	5314.77 ± 0.18	1.40 ± 0.09	15.0	2.11	3.0806	O I λ 1302	1.17
101.....	5319.94 ± 0.29	1.93 ± 0.27	7.2	2.11
102.....	5322.81 ± 0.31	2.80 ± 0.16	17.0	2.11
103.....	5325.73 ± 0.21	2.23 ± 0.24	9.1	2.11	3.3803	H I λ 1215	0.68
104.....	5337.93 ± 0.39	0.62 ± 0.10	6.2	1.14
105.....	5345.11 ± 0.10	2.17 ± 0.08	26.2	1.14
106.....	5357.77 ± 0.45	0.88 ± 0.16	5.5	2.97
107.....	5360.98 ± 0.17	2.21 ± 0.15	14.3	2.97
108.....	5369.58 ± 0.18	1.22 ± 0.09	13.6	1.77	3.5121	Si II λ 1190	−1.65
109.....	5379.48 ± 0.20	1.76 ± 0.14	12.3	4.48
110.....	5382.72 ± 0.30	1.22 ± 0.15	8.2	4.48	3.5121	Si II λ 1193	−1.48
111.....	5389.87 ± 0.18	1.27 ± 0.09	14.1	4.48
112.....	5402.29 ± 0.13	2.86 ± 0.17	16.6	6.37
113.....	5405.42 ± 0.26	2.74 ± 0.14	19.2	6.37
114.....	5408.48 ± 0.46	1.07 ± 0.23	4.7	6.37	3.5343	Si II λ 1193	−2.27
115.....	5424.81 ± 0.14	1.94 ± 0.09	22.2	3.39
116.....	5429.30 ± 0.23	1.72 ± 0.12	14.1	3.39
117.....	5432.68 ± 0.11	3.01 ± 0.12	25.6	3.39
118.....	5437.99 ± 0.11	2.17 ± 0.08	25.9	3.39
119.....	5442.61 ± 0.08	2.99 ± 0.07	43.0	3.39	3.5343	N I λ 1200	1.44
120.....	5447.20 ± 0.06	3.20 ± 0.06	49.3	3.39
121.....	5460.14 ± 0.09	3.09 ± 0.09	34.8	2.07
122.....	5464.22 ± 0.24	1.85 ± 0.13	14.4	2.07
123.....	5467.67 ± 0.13	3.24 ± 0.11	30.7	2.07
124.....	5471.71 ± 0.17	1.71 ± 0.11	16.0	2.07	3.5343	Si III λ 1206 ^c	1.06
125.....	5481.19 ± 0.37	0.70 ± 0.10	7.2	2.07
126.....	5485.42 ± 0.10	2.41 ± 0.08	31.7	2.07	3.5121	H I λ 1215	0.24
127.....	5491.43 ± 0.14	1.41 ± 0.08	18.0	2.07
128.....	5508.38 ± 0.15	1.93 ± 0.11	18.1	4.65
129.....	5511.67 ± 0.11	3.23 ± 0.07	48.3	4.65	3.5343	H I λ 1215	−0.56
130.....	5515.11 ± 0.09	3.31 ± 0.07	47.8	4.65	3.5375	H I λ 1215	−0.96
131.....	5518.95 ± 0.08	2.89 ± 0.07	42.7	4.65
132.....	5523.33 ± 0.06	2.90 ± 0.06	48.2	4.65
133.....	5535.77 ± 0.12	1.43 ± 0.07	20.7	6.15
134.....	5541.63 ± 0.08	2.13 ± 0.06	35.7	6.15
135.....	5547.37 ± 0.08	2.97 ± 0.09	32.2	6.15
136.....	5550.83 ± 0.23	1.75 ± 0.09	18.6	6.15
137.....	5554.24 ± 0.12	2.92 ± 0.08	34.4	6.15
138.....	5558.06 ± 0.10	2.38 ± 0.08	29.0	6.15
139.....	5566.40 ± 0.10	2.30 ± 0.08	27.4	3.44
140.....	5570.14 ± 0.15	2.34 ± 0.09	26.3	3.44
141.....	5573.37 ± 0.10	2.66 ± 0.11	24.8	3.44	3.5845	H I λ 1215	0.17
142.....	5583.63 ± 0.08	1.61 ± 0.05	32.2	2.90
143.....	5598.17 ± 0.14	0.94 ± 0.05	18.0	4.16
144.....	5603.32 ± 0.06	1.89 ± 0.04	42.2	4.16
145.....	5613.01 ± 0.09	1.38 ± 0.04	31.5	2.89

TABLE 3—*Continued*

Line	λ_{vac} (Å)	Equivalent Width (Å)	SL ^a	χ^2_{ν}	Redshift	Identification	Residual (Å)
146.....	5617.78 ± 0.07	1.71 ± 0.04	41.6	2.89
147.....	5623.53 ± 0.13	0.86 ± 0.04	20.1	2.89	3.6255	H I λ 1215	0.44
148.....	5642.53 ± 0.63	0.20 ± 0.05	3.9	1.54
149.....	5654.37 ± 0.59	0.23 ± 0.06	4.2	1.23
150.....	5666.50 ± 0.41	0.36 ± 0.06	5.9	2.64
151.....	5671.50 ± 0.66	0.25 ± 0.07	3.8	2.29
152.....	5684.21 ± 0.54	0.29 ± 0.07	4.3	1.83	3.5121	Si II λ 1260	−2.89
153.....	5698.59 ± 0.34	0.50 ± 0.07	7.3	4.11	3.5845	N V λ 1242	0.99
154.....	5722.28 ± 0.38	0.47 ± 0.07	6.4	1.27	3.5375	Si II λ 1260	3.15
155.....	5745.77 ± 0.50	0.35 ± 0.07	4.7	4.34	3.6255	N V λ 1242	−2.83
156.....	5773.76 ± 0.61	0.34 ± 0.08	4.0	2.31
157.....	5784.21 ± 0.44	0.47 ± 0.08	5.6	1.32
158.....	5843.33 ± 0.63	0.38 ± 0.09	4.1	1.93	3.3803	C II λ 1334	−2.38
159.....	5893.85 ± 0.75	0.41 ± 0.11	3.6	9.46
160.....	5908.54 ± 0.68	0.38 ± 0.11	3.6	1.09	3.5375	O I λ 1302	−0.01
161.....	5931.31 ± 0.62	0.42 ± 0.11	3.9	4.10
162.....	5943.54 ± 0.59	0.53 ± 0.12	4.2	0.82
163.....	6051.23 ± 0.86	0.36 ± 0.11	3.1	9.27	3.5343	C II λ 1334	0.05
164.....	6091.22 ± 0.75	0.37 ± 0.12	3.1	0.26
165.....	6102.43 ± 0.68	0.44 ± 0.12	3.6	3.67	3.3803	Si IV λ 1393	−2.69
166.....	6134.98 ± 0.51	0.56 ± 0.12	4.6	1.67
167.....	6197.15 ± 0.38	0.76 ± 0.12	6.3	3.63
168.....	6219.63 ± 0.71	0.43 ± 0.13	3.4	3.66
169.....	6232.09 ± 0.70	0.46 ± 0.13	3.6	2.46	3.0806	Si II λ 1526	2.24
170.....	6239.56 ± 0.64	0.49 ± 0.13	3.8	2.46
171.....	6270.79 ± 0.87	0.51 ± 0.15	3.5	9.87
172.....	6276.90 ± 0.70	0.49 ± 0.13	3.7	2.46
173.....	6319.79 ± 0.36	1.13 ± 0.15	7.7	1.63	3.0806	C IV λ 1548 ^f	2.23
174.....	6324.51 ± 0.82	0.56 ± 0.16	3.5	1.63	3.5375	Si IV λ 1393	0.39
175.....	6329.03 ± 0.67	0.60 ± 0.15	4.1	2.32	3.0806	C IV λ 1550	0.97
176.....	6361.86 ± 0.35	0.92 ± 0.13	7.1	3.78	3.5343	Si IV λ 1402 ^g	1.27
177.....	6397.67 ± 0.42	0.75 ± 0.13	5.7	1.72
178.....	6407.33 ± 1.01	0.39 ± 0.14	2.8	1.19
179.....	6412.12 ± 1.03	0.37 ± 0.15	2.5	1.19
180.....	6447.66 ± 0.98	0.44 ± 0.14	3.1	8.76	3.6255	Si IV λ 1393	0.83
181.....	6464.44 ± 0.57	0.51 ± 0.13	4.0	1.35
182.....	6529.01 ± 0.66	0.48 ± 0.14	3.5	2.24
183.....	6559.21 ± 0.73	0.51 ± 0.14	3.5	1.97
184.....	6583.63 ± 0.69	0.57 ± 0.16	3.6	0.61
185.....	6608.28 ± 0.68	0.58 ± 0.16	3.5	1.06
186.....	6781.64 ± 0.41	1.07 ± 0.18	5.8	1.42	3.3803	C IV λ 1548	−0.01
187.....	6795.04 ± 0.54	0.93 ± 0.18	5.2	3.32	3.3803	C IV λ 1550	2.12

^a Significance of the line defined as W/σ_W .^b Also identified at $z = 3.5375$ as C II λ 1036 with residual -0.10 Å.^c Also identified at $z = 3.5375$ as O VI λ 1037 with residual -2.04 Å.^d Also identified at $z = 3.5375$ as N II λ 1038 with residual -1.93 Å.^e Also identified at $z = 3.5375$ as Si III λ 1206 with residual -2.75 Å.^f Also identified at $z = 3.5343$ as Si IV λ 1393 with residual 0.07 Å.^g Also identified at $z = 3.5375$ as Si IV λ 1402 with residual -3.17 Å.

the fact that there is significant blending with other Ly α features, and for this reason these identifications are not listed in the tables.

3.2.2. Ly α Lines

All lines identified with metal line absorption systems in the “Ly α -only” region were removed from the line lists and the remaining lines for each component are assumed to be Ly α and make up the sample used in the following analyses. The mean redshift of the Ly α sample is 3.218 with a range of $2.903 \leq z \leq 3.534$. For the “Ly α -only” region the mean $1\sigma_{\text{lim}}$ for A–D are 0.059, 0.052, 0.034, and 0.22 Å, respectively. The line lists are complete to 0.32 Å for A and B, to 0.16 Å for C, but only to 0.99 Å for D for lines with $W \geq 4.5\sigma_{\text{lim}}$. The limiting rest equivalent width, $1\sigma_{\text{lim}}$, here is different from $1\sigma_W$ used to establish line lists in § 3 in that σ_W is the error in the equivalent width assigned to a line by the line-fitting software. The number of observed $4.5\sigma_{\text{lim}}$

lines for each component is A, 55, B, 57, C, 80, and D, 1; however, it is not possible to compare the observed number of lines to the number expected based on other work on dN/dz as these studies are made at much higher resolution.

3.3. Comparison of the Spectra

Coherent structures may be defined by the coincidence of absorption features between lines of sight. Comparison of the strengths of the lines and their separation in velocity can probe the level of homogeneity and dynamic structure of the absorbers. Images of components A and C have the maximum angular separation of $1''.31$, corresponding to the maximum transverse distance probed of $140 h_{100}^{-1}$ pc at $z = 2.9$, or the redshift of Ly α at Ly β emission for the redshift of the quasar. B and C have an angular separation of $0''.826$ and probe a transverse distance of $86 h_{100}^{-1}$ pc; and A and B are separated by $0''.512$ having the smallest transverse distance of $53 h_{100}^{-1}$ pc. Components C and D have a similar

TABLE 4
LINE LIST FOR B1422+231: COMPONENT D

Line	λ_{vac} (Å)	Equivalent Width (Å)	SL ^a	χ^2_v	Redshift	Identification	Residual (Å)
1.....	4584.14 ± 0.54	2.27 ± 0.49	4.6	2.19
2.....	4593.14 ± 0.30	3.53 ± 0.38	9.2	2.19
3.....	4598.43 ± 0.29	3.43 ± 0.41	8.4	2.19
4.....	4611.70 ± 0.33	3.20 ± 0.42	7.7	1.74
5.....	4630.12 ± 0.30	3.51 ± 0.41	8.6	2.11	3.5121	H I λ 1025	2.00
6.....	4652.52 ± 0.16	5.16 ± 0.33	15.4	3.21	3.5343	H I λ 1025 ^b	1.58
7.....	4660.87 ± 0.33	3.37 ± 0.42	8.0	3.21
8.....	4681.84 ± 0.48	2.72 ± 0.48	5.7	0.54
9.....	4688.34 ± 0.47	2.65 ± 0.50	5.4	0.54
10.....	4703.16 ± 0.38	2.70 ± 0.44	6.2	2.34	3.5845	H I λ 1025	0.77
11.....	4732.65 ± 0.28	3.38 ± 0.39	8.7	1.93
12.....	4746.90 ± 0.57	2.19 ± 0.44	5.0	1.38	3.6255	H I λ 1025	2.41
13.....	4751.37 ± 0.28	3.71 ± 0.38	9.9	1.38
14.....	4771.25 ± 0.43	2.40 ± 0.39	6.1	1.48
15.....	4794.74 ± 0.25	3.39 ± 0.32	10.6	2.07
16.....	4814.79 ± 0.26	3.62 ± 0.31	11.5	1.06
17.....	4819.38 ± 0.52	2.10 ± 0.40	5.2	1.06
18.....	4824.85 ± 0.25	3.59 ± 0.33	11.0	1.06
19.....	4829.81 ± 0.24	3.68 ± 0.32	11.3	1.06
20.....	4859.74 ± 0.53	2.14 ± 0.45	4.8	0.80
21.....	4878.01 ± 0.63	1.92 ± 0.50	3.8	1.00
22.....	4886.33 ± 0.57	2.19 ± 0.50	4.4	0.61
23.....	4904.08 ± 0.69	1.94 ± 0.52	3.8	1.44
24.....	4935.92 ± 0.66	1.83 ± 0.49	3.7	0.47
25.....	4948.39 ± 0.38	2.89 ± 0.43	6.7	0.49
26.....	4967.89 ± 0.27	3.49 ± 0.40	8.7	2.64
27.....	4975.32 ± 0.26	3.69 ± 0.39	9.5	2.64
28.....	4991.13 ± 0.66	1.83 ± 0.46	4.0	1.47
29.....	5004.77 ± 0.43	2.89 ± 0.46	6.3	1.18
30.....	5012.38 ± 0.60	2.13 ± 0.53	4.0	1.18
31.....	5022.44 ± 0.28	4.20 ± 0.49	8.7	2.33
32.....	5028.18 ± 0.30	3.77 ± 0.45	8.3	2.33
33.....	5036.17 ± 0.55	2.56 ± 0.58	4.4	0.46
34.....	5053.11 ± 0.51	2.79 ± 0.52	5.4	1.25
35.....	5091.58 ± 0.39	3.07 ± 0.52	5.9	1.24
36.....	5135.36 ± 0.59	2.44 ± 0.56	4.4	0.59
37.....	5170.00 ± 0.30	3.74 ± 0.46	8.2	3.25
38.....	5183.09 ± 0.45	2.65 ± 0.50	5.3	1.12
39.....	5197.89 ± 0.41	2.93 ± 0.47	6.3	0.63
40.....	5251.61 ± 0.44	3.15 ± 0.53	5.9	1.23
41.....	5264.11 ± 0.51	2.85 ± 0.56	5.1	0.53
42.....	5277.87 ± 0.42	3.11 ± 0.54	5.8	0.70
43.....	5304.60 ± 0.57	2.40 ± 0.54	4.5	0.69
44.....	5323.00 ± 0.23	4.84 ± 0.37	12.9	0.62	3.3803	H I λ 1215	-2.05
45.....	5338.03 ± 0.65	2.13 ± 0.54	3.9	0.47
46.....	5346.31 ± 0.76	1.94 ± 0.55	3.5	1.68
47.....	5360.61 ± 0.45	2.83 ± 0.50	5.6	0.97
48.....	5403.75 ± 0.27	4.15 ± 0.44	9.5	0.74
49.....	5428.92 ± 0.40	3.38 ± 0.48	7.0	1.24
50.....	5434.34 ± 0.38	3.51 ± 0.48	7.4	1.24
51.....	5446.82 ± 0.34	3.57 ± 0.47	7.6	2.67
52.....	5460.97 ± 0.37	3.57 ± 0.48	7.4	0.87
53.....	5468.60 ± 0.42	3.06 ± 0.52	5.9	0.87
54.....	5485.14 ± 0.66	1.72 ± 0.48	3.6	1.51	3.5121	H I λ 1215	-0.04
55.....	5510.97 ± 0.24	4.05 ± 0.33	12.3	1.52
56.....	5515.30 ± 0.41	3.65 ± 0.43	8.4	1.52	3.5375	H I λ 1215 ^c	-0.77
57.....	5518.93 ± 0.51	3.06 ± 0.46	6.6	1.52
58.....	5523.42 ± 0.37	2.95 ± 0.38	7.8	1.52
59.....	5541.85 ± 0.40	2.25 ± 0.35	6.4	0.56
60.....	5548.44 ± 0.26	3.22 ± 0.30	10.9	0.56
61.....	5553.65 ± 0.25	3.64 ± 0.28	12.8	0.56
62.....	5557.92 ± 0.38	2.69 ± 0.35	7.7	0.56
63.....	5567.75 ± 0.34	2.64 ± 0.34	7.9	0.56
64.....	5572.61 ± 0.22	3.64 ± 0.27	13.5	0.56	3.5845	H I λ 1215	-0.59
65.....	5598.68 ± 0.59	1.13 ± 0.26	4.3	0.86
66.....	5604.03 ± 0.34	1.84 ± 0.22	8.2	0.86
67.....	5612.87 ± 0.44	1.28 ± 0.22	5.7	0.39
68.....	5618.35 ± 0.38	1.42 ± 0.21	6.7	0.39
69.....	5641.69 ± 0.51	1.07 ± 0.22	4.8	0.87
70.....	5702.03 ± 0.74	1.12 ± 0.33	3.4	1.00
71.....	5718.38 ± 0.60	1.48 ± 0.33	4.4	2.15

TABLE 4—Continued

Line	λ_{vac} (Å)	Equivalent Width (Å)	SL ^a	χ^2_v	Redshift	Identification	Residual (Å)
72.....	5724.95 ± 0.71	1.21 ± 0.34	3.5	0.49
73.....	5880.76 ± 0.68	2.07 ± 0.54	3.8	0.32
74.....	6077.88 ± 0.52	2.51 ± 0.56	4.5	1.39
75.....	6547.43 ± 0.69	2.62 ± 0.76	3.4	0.51
76.....	6791.89 ± 0.60	3.35 ± 0.77	4.4	0.98
77.....	6801.98 ± 0.40	4.15 ± 0.69	6.0	1.90

^a Significance of the line defined as W/σ_W .

^b Also identified at $z = 3.5375$ as H I $\lambda 1025$ with residual -1.66 Å.

^c Also identified at $z = 3.5343$ as H I $\lambda 1215$ with residual 3.07 Å.

angular separation to that of C and A of $1''.29$, but D is ~ 23 times fainter than the other images and its low SNR spectrum renders it not useful for comparisons. The absorption features that make up the samples used in the following analyses probe lookback times that are 87%–90% of the age of the universe.

3.3.1. Line Coincidences and Anticoincidences

The selection criteria for the sample of lines used in testing for intrinsic differences in line strength across the lines of sight is based on central wavelength, line strength and identification. Because of the difficulty in identifying higher order Lyman lines blueward of Ly β , we defined in § 3.1.1 the “Ly α -only” region as the range in wavelength from Ly β at the emission redshift of the quasar to Ly α emission less an increment in redshift, which corresponds to 6000 km s^{-1} to avoid the absorbers affected by the proximity effect (Bechtold 1994). Any line in this region having a significance (SL) as listed in Tables 1–4 of less than 5 is removed from the sample, and lines identified as metals are removed from the Ly α list and form a line list that will be analyzed separately. There are 64, 70, and 81 Ly α lines for A paired to C, B paired to C, and A paired to B, hereafter denoted as AC, BC, and AB, respectively. The metal line lists contain 9, 9, and 12 lines for A–C, respectively.

Coincidences are defined by pairing lines in components A and B to the lines in the C component because it has the highest SNR and therefore, we expect it to have the most reliable line measurements. Since B has the second highest SNR, and hence a few more lines than A, lines in A are paired to those in B. Each line in A and B is paired with a line in C, and each line in A is paired with a line in B by choosing the single nearest neighbor in velocity. Consequently, for the Ly α lines there are 62 AC pairs, 68 BC pairs, and 62 AB pairs. To evaluate the number of anti-

coincidences the opposite approach is taken where lines in the reference spectrum C are compared to lines in the comparison spectrum A and B, and lines in the reference spectrum B are compared to lines in comparison spectrum A to find lines that were not paired by the previous procedure. To determine whether these lines are anticoincidences or if they simply fall below the detection threshold of the lower SNR spectrum, we define an anticoincidence to be a situation where the equivalent width of an unpaired line in the reference spectrum minus $2\sigma_{\text{rms}}$ (the rms scatter in the equivalent widths of the paired lines plotted against each other) of the comparison spectrum is greater than $5\sigma_{\text{lim}}$ for the comparison spectrum. With this definition, the following number of anticoincident Ly α lines are found: 3 for AC, 1 for BC, and 1 for AB.

The number of coincidences and anticoincidences can be found for the metal lines using the same procedure. The number of coincidences is 8 for AC, 9 for BC, and 8 for AB. The number of anticoincidences is 1 for each of the paired lines of sight AC, BC, and AB; however, given that each of these occurs in a heavily blended feature and that narrow metal lines are certainly blended with one or more Ly α lines, the classification of anticoincidence is considered to be highly uncertain.

Figure 3a displays comparisons of the rest equivalent widths of the Ly α lines for the AC, BC, and AB pairs; they are highly correlated. All pairs match within 100 km s^{-1} , and the rms scatter about the linear relationship with slope unity is 0.048 Å for A vs. C, 0.052 Å for B vs. C, and 0.055 Å for A vs. B—these are on the order of the propagated errors in the rest equivalent widths between the paired lines of sight. For a line in A or B matching a line in C within 100 km s^{-1} , the probability that the coincidence is random is 0.45, and this decreases to 0.27, 0.13, and 0.04 for smaller match ranges of 60, 30, and 10 km s^{-1} . However, plots made for pairs with velocity splittings less than 60, 30, and 10 km s^{-1} exhibit a decrease in the number of pairs without a significant decrease in rms. This indicates that the lost pairs are real pairs because had they been random pairs, an improvement in the rms would have been evident as the match range narrows. The high degree of correlation (coefficients of $R = 0.93$ for A vs. C, $R = 0.91$ for B vs. C, $R = 0.89$ for A vs. B) is a sign that far fewer than 45% of the matches within the 100 km s^{-1} are spurious.

The equivalent widths for the metal line pairs are compared in Figure 3b. All pairs for A vs. C, B vs. C, and A vs. B match with 75 km s^{-1} , except one pair in BC that has a Δv of 146 km s^{-1} and the greatest difference in equivalent width; the rms scatter is 0.079, 0.066, and 0.055 Å , respectively. As for the Ly α lines the rms does not improve with a

TABLE 5
METAL LINE SYSTEMS FOR B1422+231

Redshift (z)	Lines ^a	Published z ^b	A ^c	B ^c	C ^c	D ^c
3.0806 ± 0.0017.....	5	3.091	4	3	6	0
3.3803 ± 0.0014.....	4	3.382	3	2	7	1
3.5121 ± 0.0008.....	6	3.515	5	5	5	2
3.5343 ± 0.0006.....	2	3.536	5	8	12	2
3.5375 ± 0.0011.....	2	3.538	4	7	11	2
3.5845 ± 0.0002.....	2	3.587	3	2	3	2
3.6255 ± 0.0005.....	2	3.624	2	1	4	1

^a The number of lines used to determine the systemic redshift.

^b Bechtold & Yee 1995.

^c The number lines identified with the metal line system for this component of B1422+231.

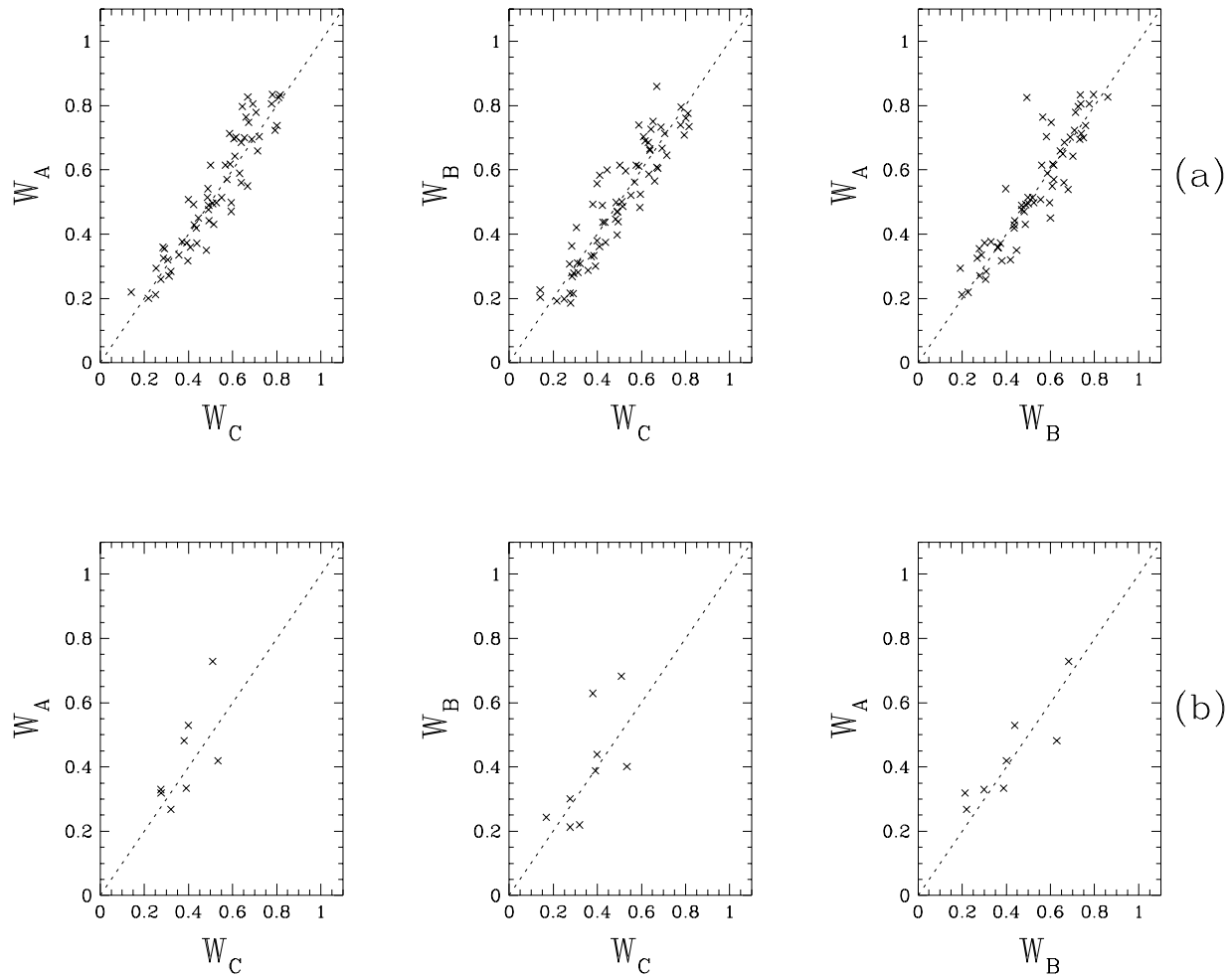


FIG. 3.—(a) Rest equivalent widths for the Ly α lines for AC, BC, and AB. The rms of the scatter is 0.048, 0.052, and 0.055 Å, respectively. (b) Rest equivalent widths for the metal line pairs for AC, BC, and AB. The rms of the scatter is 0.079, 0.086, and 0.056 Å, respectively.

narrows the velocity match range, illustrating that the pairs are real rather than random pairs. A definite correlation is observed (coefficients of $R = 0.68$ for A vs. C, $R = 0.69$ for B vs. C, $R = 0.88$ for A vs. B) but any interpretation is limited because of the low resolution of the FOS data and the high degree of blending.

3.3.2. Variations of Absorption Line Strength

Having identified coincidences of absorption lines across the lines of sight for both Ly α and metal lines, the data are examined for differences in the equivalent widths due to intrinsic variations which exceed that expected from noise. Figure 4 shows for paired lines of sight AC, BC, and AB histograms of the differences in the rest equivalent widths for each line pair divided by the errors in the two measurements added in quadrature. If the differences between the line pairs is due solely to measurement error, this distribution will be consistent with a Gaussian having unit sigma. The overplotted curves are unit Gaussians scaled to the area of the histogram and centered on the expected mean of zero. For the Ly α lines (Fig. 4a) the histograms appear to be Gaussian but slightly broader than unit sigma and there are no outliers beyond 4.5σ . These results hold for similar plots (not shown) made for subsets of lines with subsequently smaller velocity separations (60, 30, and 10 km s $^{-1}$) until at the low end the Gaussian fit is subject to small number statistics as the number of pairs drops. For the metal lines

the histograms are consistent with the Gaussian but the shape of the distribution is more difficult to discern because of the small number of pairs. A χ^2_ν comparison of either the Ly α or metal line histograms to the unit Gaussian is of limited value because of the small size of the data sample and the loss of information that occurs during binning.

A different approach to detecting differences in equivalent widths of the line pairs is to use a maximum-likelihood technique, which has the advantage of quantifying the level to which any differences may be detected. This method begins by describing the probability that a system will exist in a particular state in terms of the variable of interest. The presumption that the system is observed in its most likely state implies that the maximum of the probability function gives the most likely value for the variable. If the probability of measuring a pair of lines with equivalent width difference Δ and propagated error ϵ is $P(\Delta, \epsilon)$, then the probability \mathcal{M} of measuring a set of N pairs of lines each with particular values Δ_i and ϵ_i is the product of the individual probabilities, $P(\Delta_i, \epsilon_i)$:

$$\mathcal{M} = \prod_{i=0}^N P(\Delta_i, \epsilon_i). \quad (1)$$

The distribution of equivalent width differences for the i th pair of lines may be represented by a Gaussian with a mean of zero and with a dispersion given by the combination in

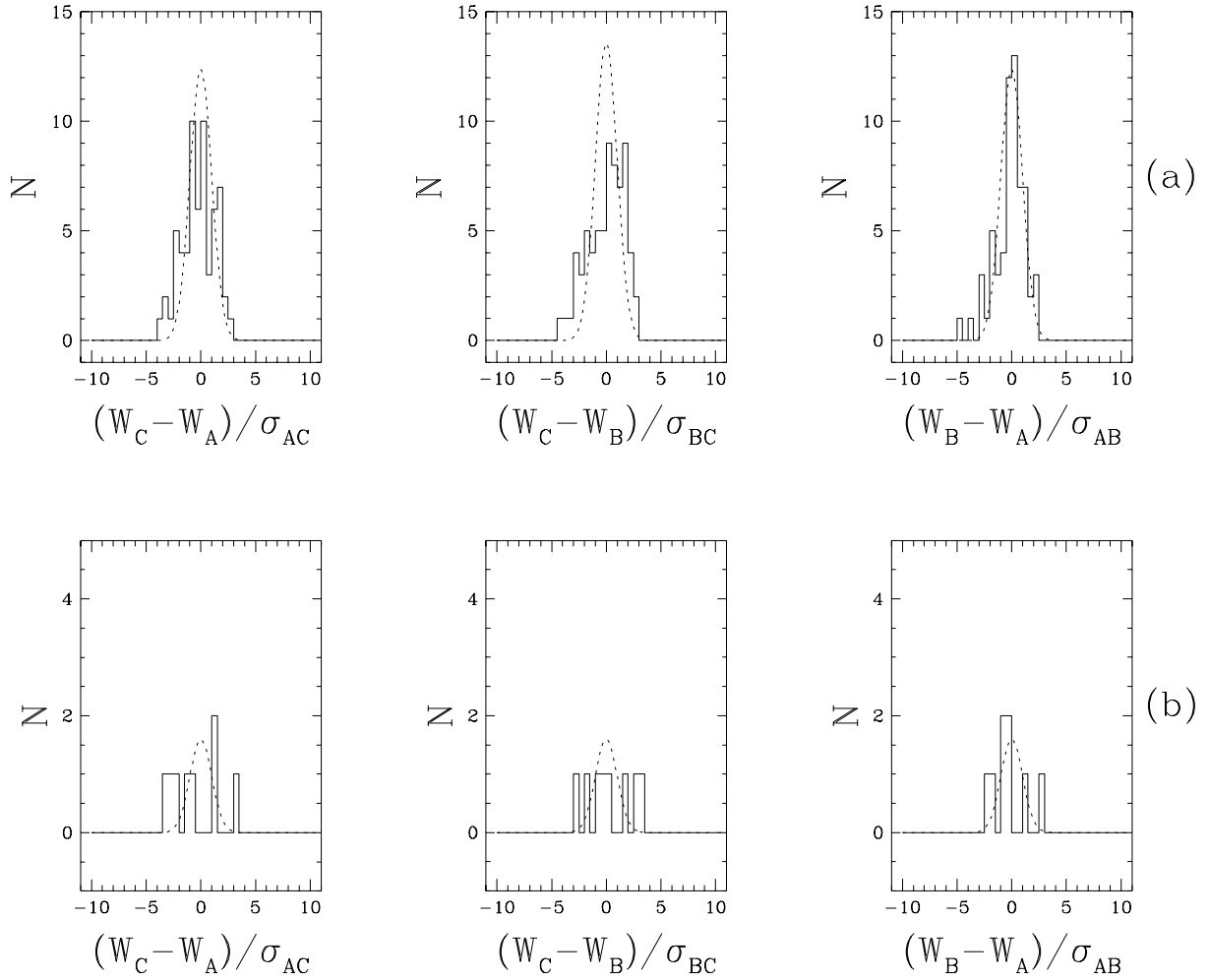


FIG. 4.—Histograms of the difference in the rest equivalent widths for pairs of lines AC, BC, and AB, which have been divided by their errors added in quadrature for (a) the Ly α pairs and (b) the metal line pairs. The overplotted curve is a unit sigma Gaussian centered on zero and scaled to the area under the histogram.

quadrature of the measurement errors, ϵ_i . The fitted parameter is the average intrinsic difference between the pairs s and is introduced by adding in quadrature to the measurement errors:

$$\mathcal{M} = \prod_{i=1}^N \frac{1}{\sqrt{2\pi(\epsilon_i^2 + s^2)}} \exp \left[\frac{-\Delta_i^2}{2(\epsilon_i^2 + s^2)} \right]. \quad (2)$$

Because any individual probability is much less than 1, the product of a large number of these probabilities may be very small, so taking the natural logarithm of both sides of this equation avoids computational errors that may result from handling such small numbers:

$$M = \ln(\mathcal{M}) = \sum_{i=1}^N -\frac{1}{2} \ln [2\pi(\epsilon_i^2 + s^2)] - \frac{\Delta_i^2}{2(\epsilon_i^2 + s^2)}. \quad (3)$$

Using the Ly α and metal line pairs separately for each of the paired lines of sight AC, BC, and AB, the function M is computed for values of Δ_i and ϵ_i from all line pairs in the sample as a function of s . The curves for the Ly α pairs are presented in Figure 5a to give a general visual impression of the function M .

Maximizing M returns the most likely value, s_{\max} , which is the difference on average in the equivalent widths of each line pair between the lines of sight. If the sample is large enough that M is Gaussian in the vicinity of s_{\max} , then the

95% confidence interval is given for one degree of freedom (i.e., fitting one parameter) by $\Delta\chi^2 = 4.0$, which corresponds to $\Delta M = -2.0$, or where M falls by -2.0 . This is more readily seen from Figure 5b, where the relative-likelihood function, \mathcal{M}_r , which is simply \mathcal{M} normalized by its maximum value [$\mathcal{M}_r = \exp(M - M_{\max})$], is plotted. Since \mathcal{M}_r is Gaussian for a sufficiently large sample, the 2σ limits correspond to $\Delta\mathcal{M}_r = \exp(-2)$. The maximum-likelihood values for the average difference s_{\max} and the 95% confidence intervals for the Ly α lines are 0.046 ± 0.017 and 0.054 ± 0.017 Å for components A and B paired with C, respectively, and 0.044 ± 0.021 Å for A paired to B. Because of the low resolution of the FOS data the equivalent widths measured for the narrow metal lines are not reliable enough for this type of analysis to be meaningful.

The fact that the 2σ uncertainty about the average difference does not encompass zero for any of the pairs of spectra can be explained by either a real intrinsic difference between the lines of sight or by an underestimate of the errors in the equivalent widths by the line-fitting software. To determine whether the errors have been underestimated we can examine the simulated data (see Appendix) where 1000 pairs of input lines having SNR, line strength and separation comparable to that of A and B were generated and processed by the line-fitting software. The measured equivalent width and error can be compared to the input value, W_i , by

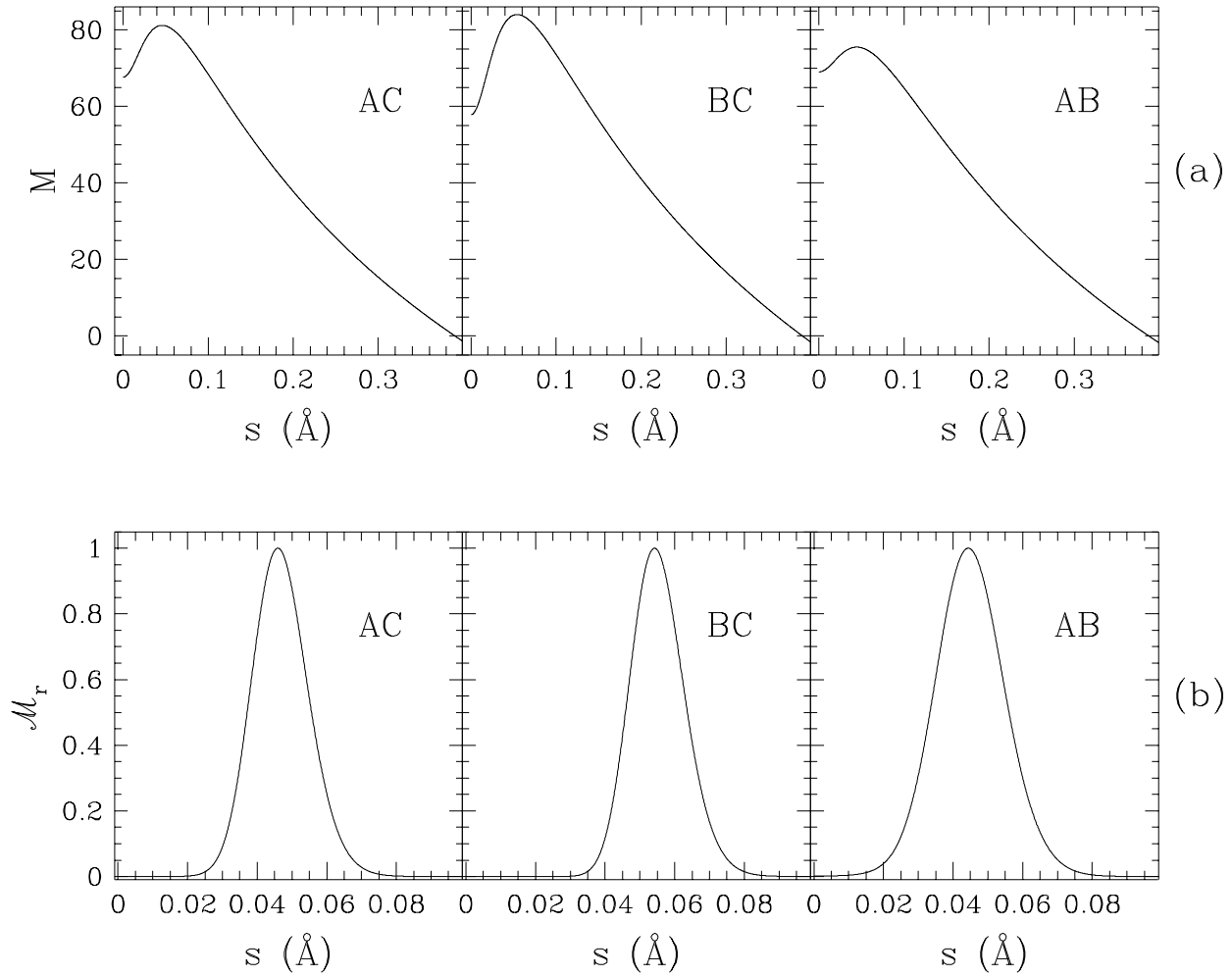


FIG. 5.—(a) Maximum-likelihood function, M , for the variable s for the Lyz lines of pairs AC, BC, and AB. (b) Relative-likelihood function $M_r = \exp(M - M_{\max})$.

plotting the distribution of $(W - W_t)/\sigma_W$ for either input line. The histograms for both input lines are presented in Figure 6 and the fact that the distribution of data is slightly broader than the unit Gaussian implies the software has underestimated the errors in the equivalent widths.

The maximum-likelihood technique can be used to find the amount of difference from the expected unit Gaussian

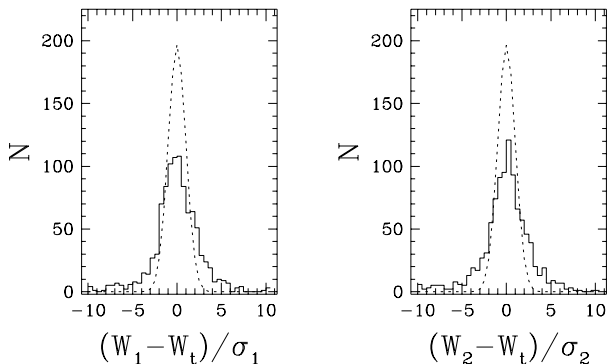


FIG. 6.—Histograms of the difference between the rest equivalent width and the true equivalent width for each of the two lines input to the simulated data divided by the error. The dashed curve is a unit sigma Gaussian centered on zero scaled to the area under each histogram.

(in the form of addition in quadrature to the errors, s_{\max}), which is 0.0468 ± 0.0034 Å for the first input line and 0.0480 ± 0.0036 Å for the second input line, and these are greater than the values of s_{\max} obtained for the real data pairs to within the errors. The maximum-likelihood technique can also be performed in terms of a factor of increase, x , in the equivalent width errors by substituting $(x\epsilon_i)^2$ for $(\epsilon_i^2 + s^2)$ in equations (2) and (3). So for the simulated data x_{\max} is 1.846 ± 0.091 and 1.888 ± 0.092 for input lines 1 and 2, respectively, and this translates into an underestimate in the equivalent width errors of $45.8^{+2.5}_{-2.8}\%$ and $47.0^{+2.5}_{-2.7}\%$. The real data pairs are processed in the same way and x_{\max} is found to be 1.495 ± 0.315 , 1.688 ± 0.337 , and 1.410 ± 0.297 for paired lines of sight AC, BC, and AB, respectively. This can be translated into an underestimate in the errors of $33^{+12}_{-18}\%$, $41^{+10}_{-15}\%$, and $29^{+12}_{-19}\%$ for pairs AC, BC, and AB, respectively. Since these numbers are smaller than the underestimate in the errors derived from the simulated data, we conclude that the broadening of the distributions is due to an underestimate of the equivalent width errors and not to intrinsic differences in the equivalent widths across the lines of sight.

These results allow us to compute the smallest variation in equivalent width we could have detected using the above technique from the average errors in the equivalent widths of the real data in two ways: as a percentage of an average

line and as a column density. The upper bound on the smallest variation detectable between each pair of lines of sight is given by the value of s_{\max} plus its 2σ error, which is 0.063, 0.071, and 0.065 Å for AC, BC, and AB, respectively. This implies that the differences in the equivalent widths across the lines of sight must *on average* be less than 13%, 15%, and 14% of the line strengths (assuming an average line strength of $\bar{W} = 2.0$ Å) for AC, BC, and AB over transverse scales 0–0.14 kpc. Assuming an unsaturated line, the upper bounds on column density inhomogeneities across the lines of sight are $\log(\Delta N_{\text{H}})$, where ΔN_{H} is in cm^{-2} , of 13.06, 13.12, and 13.08 for AC, BC, and AB, respectively. Note that a Ly α line with $W = 2.0$ Å typically has a column density $\log(N_{\text{H}}) \geq 14$, where is it just leaving the linear part of the curve of growth. In the case where $W \lesssim 2.0$ (about 50% of the lines) or where the FOS feature is a blend of unsaturated lines, the assumption of an unsaturated line profile to calculate $\log(\Delta N_{\text{H}})$ is probably very good. For features that are composed of some fraction of barely saturated or fully saturated lines, the values of $\log(\Delta N_{\text{H}})$ will be lower limits, and the true values will depend on whether the feature is composed of blended saturated features and if so how many, and to what degree the individual components are saturated—these quantities cannot be determined with this data.

This level of variation is about a factor of 3 smaller than the 50% variation in line strength found by Bechtold & Yee (1995) inferred from simulations of ground-based data of two components of B1422+231. They note that a factor of 2 increase in the equivalent width errors would be necessary to obtain a null result or no equivalent width differences between their two lines of sight. The automated line-finding software used in this work has allowed a quantitative evaluation of the equivalent width errors, and it has been shown that these errors have been underestimated by about this amount (i.e., a factor of ~ 2.2). We have chosen to use this result to adjust the errors and have subsequently placed smaller limits on the equivalent width differences between the lines of sight.

Because of the uncertainties involved with continuum fitting and line deblending in the high-redshift Ly α forest, we also implemented a method of searching for intrinsic differences in absorptivity that is independent of these issues. The spectra in the paired lines of sight were optimally scaled to a common continuum and subtracted from one another. Convolution of this residual spectrum with the instrumental profile and comparison to the propagated errors can identify possible intrinsic differences between the lines of sight. Maximum-likelihood analysis was also applied to put limits on the size of any detected variations in the flux over the wavelength range of the “Ly α -only” region.

The scale factor required to normalize the continua between lines of sight was found by dividing the spectrum into six bins and using a least-squares technique to optimize the scale factor, α , separately for each bin where the resulting spectrum is given by $C - A/\alpha_{\text{AC}}$, $C - B/\alpha_{\text{BC}}$, and $B - A/\alpha_{\text{AB}}$. The scale factor for each pair does not vary as a function of wavelength, if the central two bins that span the Ly α emission feature are omitted, and averaging the factors for the remaining four bins gives values of 1.563 ± 0.014 , 2.014 ± 0.041 , and 0.777 ± 0.014 for α_{AC} , α_{BC} , and α_{AB} , respectively. Figure 7 shows the scaled and differenced spectra for paired lines of sight AC, BC, and AB, which have

been convolved with the instrumental profile since any intrinsic differences will be spread over the width of the instrumental resolution. The 2σ propagated error is overplotted and few individual differences are seen beyond this envelope.

Maximum-likelihood analysis was performed on the scaled, differenced, and convolved spectra where the variable fit, s , is the rms of the distribution of the intrinsic flux difference between the lines of sight over a resolution element. For paired lines of sight AC, BC, and AB, s_{\max} is $7.06 \pm 0.85 \times 10^{-17}$, $5.93 \pm 0.72 \times 10^{-17}$, and $1.22 \pm 0.20 \times 10^{-16}$ ergs $\text{cm}^{-2} \text{s}^{-1} \text{Å}^{-1}$. These values are not consistent with zero so maximum-likelihood analysis is then performed on the scaled and differenced spectrum without convolution and setting up the fitted variable as x , a factor of increase in the errors. The returned values for x_{\max} are the factors by which the errors in the measured flux would have to increase for the results to be consistent with no variation across the lines of sight and are 1.188 ± 0.066 , 1.218 ± 0.068 , and 1.074 ± 0.062 . This implies that for AC, BC, and AB, respectively, only a 16%, 18%, and 6.9% underestimate in the errors is needed to account for the difference measured. The results from the convolved differenced spectra gives the 95% confidence level upper bound on flux variations of 7.91×10^{-17} , 6.65×10^{-17} , and 1.42×10^{-16} ergs $\text{s}^{-1} \text{cm}^{-2} \text{Å}^{-1}$ for AC, BC, and AC, respectively. Since this is the sum of the flux in an instrumental resolution element it may be converted to an equivalent width by scaling by the average continuum flux in C, C, and A, respectively (conservatively using the lower mean flux from each pair), which is 0.15, 0.13, and 0.17 Å. This can be interpreted as a variation on average for an average line ($\bar{W} = 2.0$ Å) of 7.5%, 6.5%, and 8.5%, which is about a factor of 2 smaller than the number established using the line pairs. Assuming an unresolved, unsaturated line this corresponds to a column density inhomogeneity of $\log(\Delta N_{\text{H}}) = 12.81, 12.74, \text{ and } 12.86$, where ΔN_{H} is in cm^{-2} for AC, BC, and AC, respectively.

3.3.3. Variations of Absorption Line Velocity

The dynamical structure of the absorbers can be investigated by examining the velocity splitting between the central wavelengths of paired lines with the same methods used to compare the line strengths. The distribution of velocity differences for the Ly α pairs for each of the paired lines of sights is shown in Figure 8. A Gaussian with width given by the measured rms and scaled to the area under the data points is overplotted. The mean and rms for the Ly α line distributions are as follows: CA: $-4.43 \pm 42.9 \text{ km s}^{-1}$; CB: $10.5 \pm 32.1 \text{ km s}^{-1}$; AB: $-15.5 \pm 28.8 \text{ km s}^{-1}$. The mean and rms for the metal line distributions are for CA: $4.18 \pm 44.5 \text{ km s}^{-1}$; for CB: $31.8 \pm 51.5 \text{ km s}^{-1}$; and for AB: $-26.6 \pm 32.7 \text{ km s}^{-1}$. Also, the distribution of velocity splittings between 1000 lines input to the simulated data (see Appendix) and the lines that were recovered by the software is shown (S2). This gives a measure of the error in the central wavelength determination that is introduced by the software. The mean and rms for the simulated data distribution is $-2.52 \pm 25.3 \text{ km s}^{-1}$.

Histograms of the ratio of the velocity difference between line pairs to the propagated error in the central wavelengths converted to velocity for the Ly α and metal line pairs are presented in Figure 9. Again, the distribution of this ratio will be a unit Gaussian if there is no difference in the line

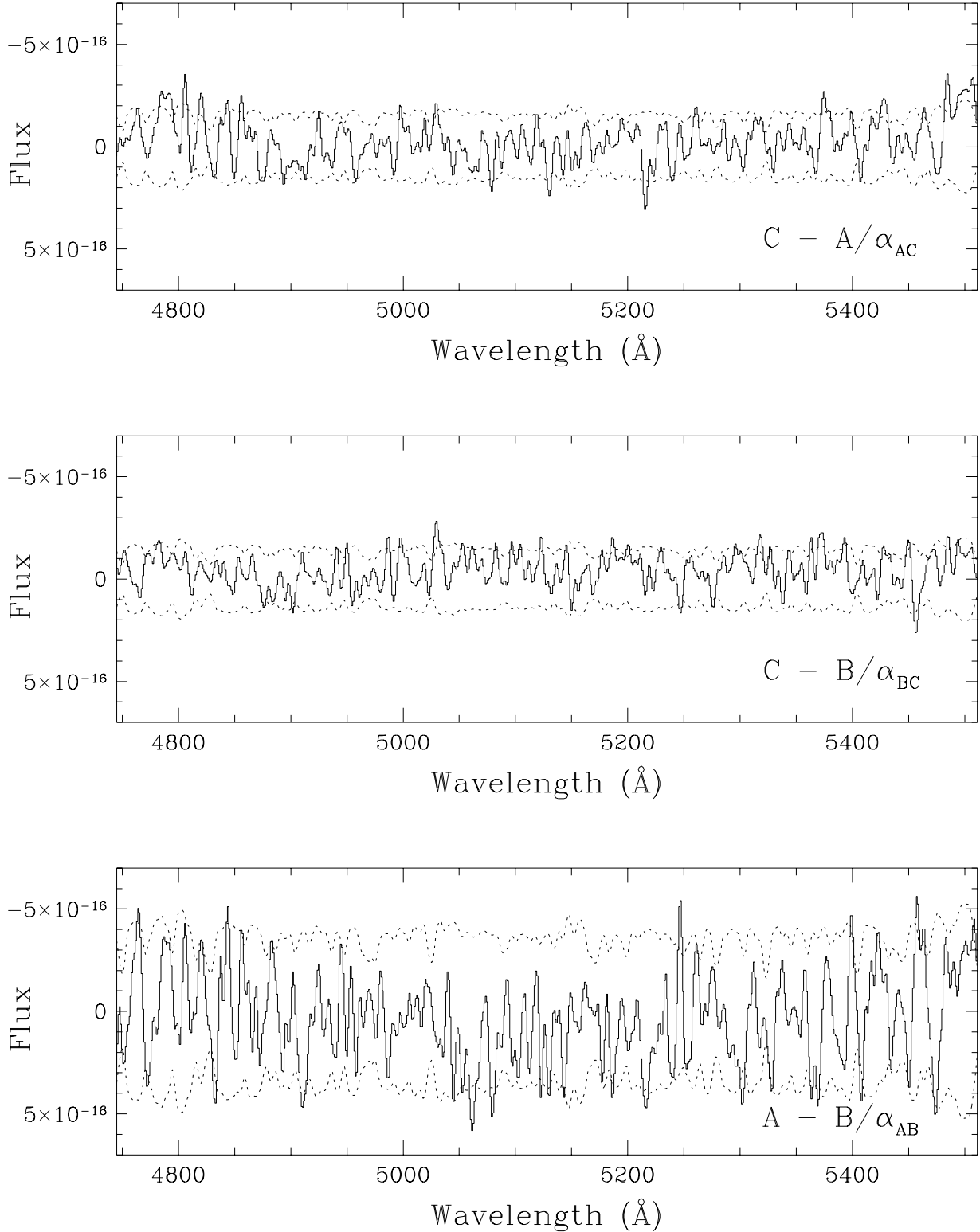


FIG. 7.—Optimally scaled and differenced spectra for paired lines of sight AC, BC, and AB, which have been convolved by the instrumental profile. The dashed curve is the scaled and propagated 2σ error; flux units are in $\text{ergs s}^{-1} \text{cm}^{-2} \text{\AA}^{-1}$.

centers beyond that of the measurement error. The histograms appear to be Gaussian but slightly broader than unit sigma and there are few outliers beyond 5σ . The amount of broadening in the distribution due to an underestimate of the error in the central wavelengths can be assessed by using the maximum-likelihood technique to find the factor by which the errors should be increased. Velocity differ-

ences greater than this could be interpreted as intrinsic differences.

Figure 10 is the distribution of the ratio of velocity differences between the input and measured line to the propagated error for each of the two input lines from the simulations. In the maximum-likelihood function, M , Δ_i is now the velocity separation of the pairs and ϵ_i is the error in the

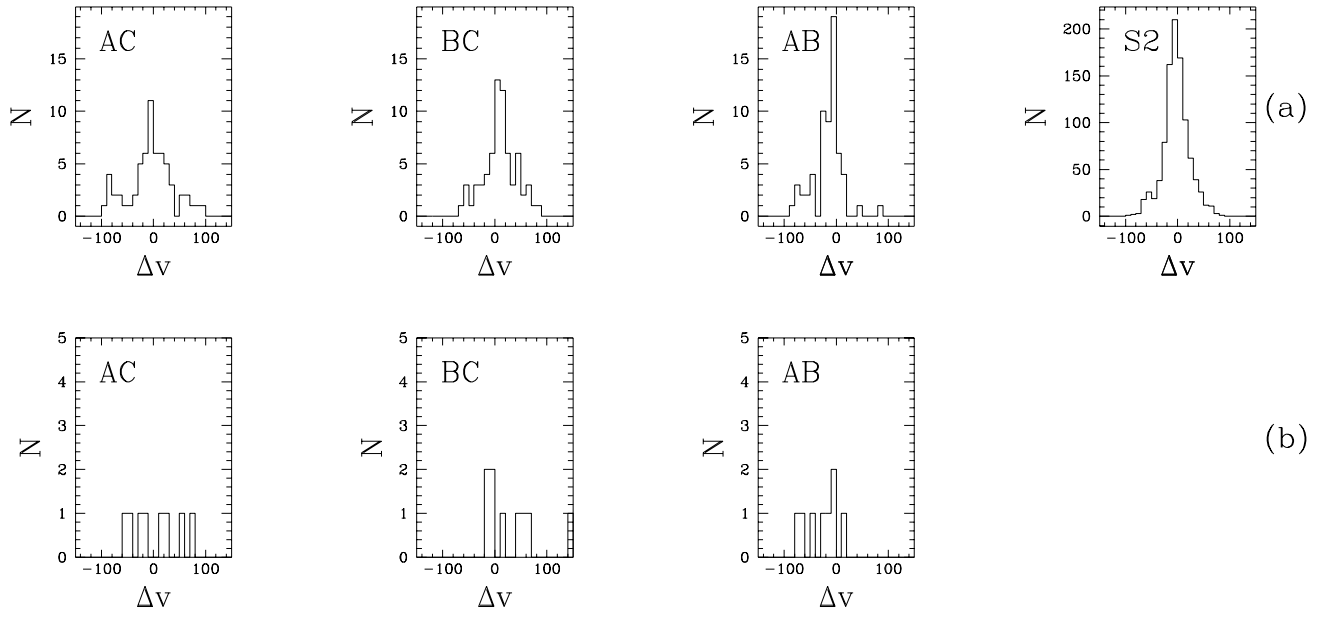


FIG. 8.—Distribution of velocity splittings for AC, BC, and AB pairs for (a) the Ly α lines and (b) the metal lines. S2 is the distribution of velocity separations between the central wavelength for the second input line in the simulated data and its line center as recovered by the software.

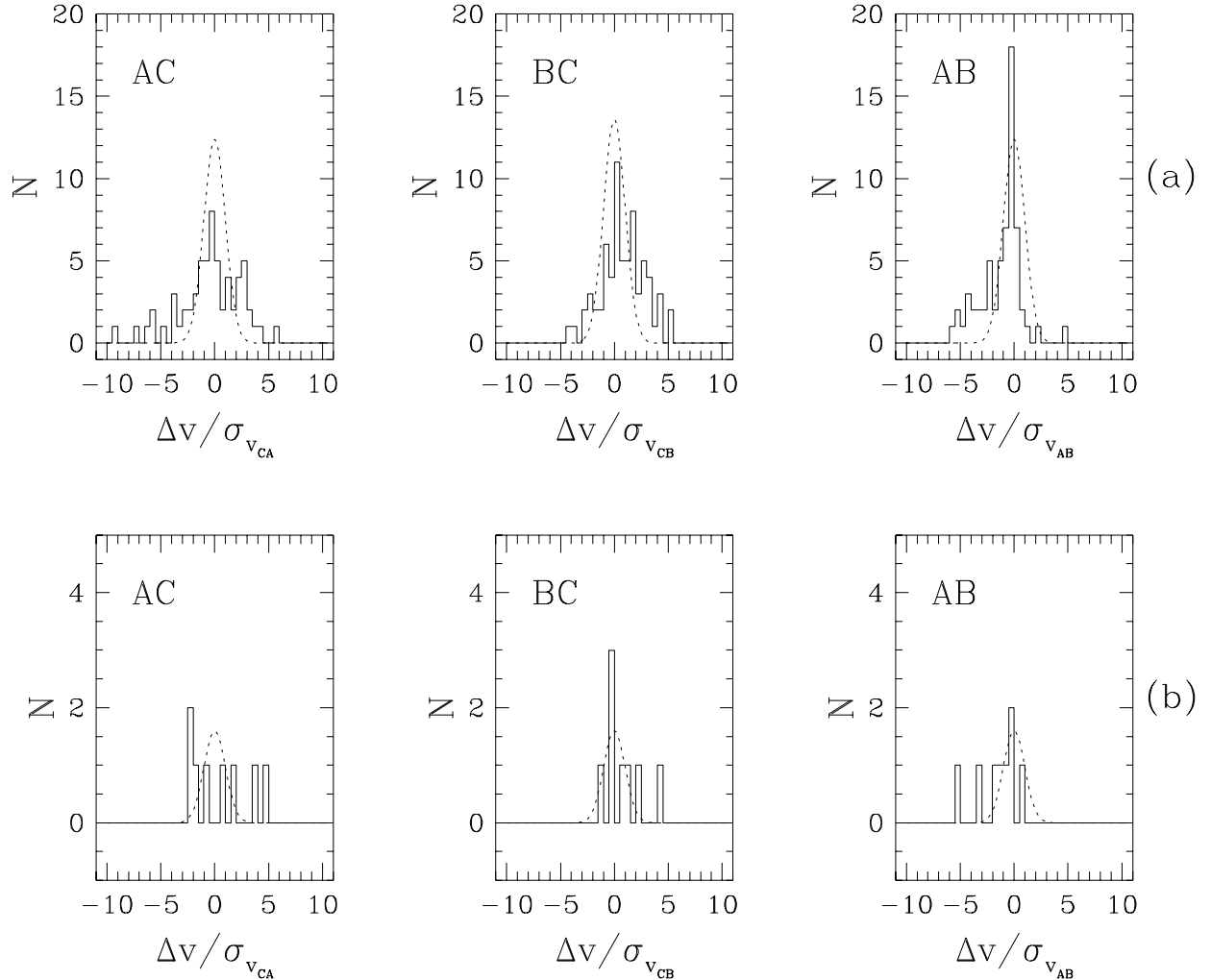


FIG. 9.—Histograms of the velocity splittings divided by the propagated error in central wavelength (in velocity units) for (a) the Ly α lines and (b) the metal lines. The dashed line is a unit sigma Gaussian centered on zero and scaled to the area under the histogram.

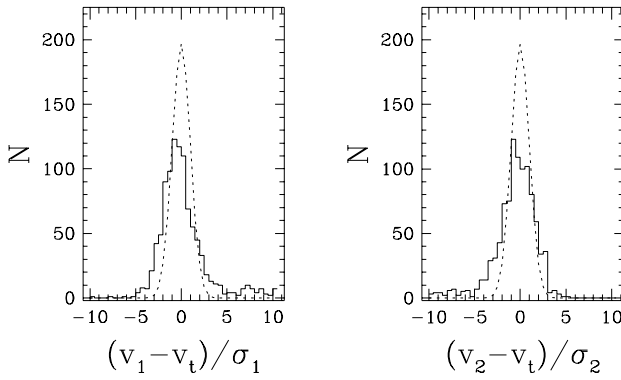


FIG. 10.—Histograms of the velocity difference between the input central wavelength for each line in the simulated data and the line center recovered by the software divided by the error in the recovered line center in velocity units. The dashed curve is a unit sigma Gaussian centered on zero and scaled to the area under each histogram.

measured line centers added in quadrature and converted to a velocity. Maximizing M to find s_{\max} , excluding the pairs with $(v - v_i)/\sigma \geq 5$ so the tails of the distribution do not dominate the fit, gives $15.0 \pm 1.2 \text{ km s}^{-1}$ and $14.9 \pm 1.2 \text{ km s}^{-1}$ for the first and second input lines. This can be translated to the factor by which the errors should be corrected by maximizing M , written in terms of x , to find x_{\max} , which is found to be 1.715 ± 0.085 and 1.721 ± 0.084 . Evaluating s_{\max} and the 2σ bounds for the Ly α pairs gives $37.8 \pm 9.6 \text{ km s}^{-1}$, $28.3 \pm 7.4 \text{ km s}^{-1}$, and $27.5 \pm 7.6 \text{ km s}^{-1}$ for pairs AC, BC, and AB, respectively. If all the broadening is due to an underestimate in the error in the central wavelengths, then evaluating x_{\max} and its 2σ errors leads to a percent underestimate of $52.5^{+8.7}_{-13.6}\%$, $50.7^{+8.3}_{-12.6}\%$, and $46.8^{+9.5}_{-14.8}\%$. These values are compared to those derived for the simulated data, and while the differences interpreted as underestimates found for the real data are slightly higher than for the simulations, they are still consistent to within the errors. This means any differences in velocity splitting that has been detected with the maximum-likelihood technique can be attributed to an underestimate in the errors.

For the metal lines the number of pairs is too small and the blending issues are too dominant to meaningfully put limits on the velocity variations between lines of sight. For the Ly α lines the upper bound on the intrinsic velocity splitting is given by s_{\max} plus the 2σ error, which is 47, 36, and 35 km s^{-1} for AC, BC, and AB, respectively. This means that variations in velocity greater these numbers have not been detected over transverse sizes $\leq 0.14 \text{ kpc}$ for the Ly α absorbers at the 95% confidence level.

4. RESULTS

Here we summarize the main observational results from the analyses of three of the four lines of sight toward the B1422+231 system that probe redshifts $2.9 \leq z \leq 3.5$ and transverse separations $0-0.14 h_{100}^{-1} \text{ kpc}$.

1. In the “Ly α -only” region ($4745-5511 \text{ \AA}$) the limiting rest equivalent width is 0.059, 0.052, 0.034, and 0.22 \AA for A–D, respectively; we identified 55, 57, 80, and one $4.5\sigma_{\text{lim}}$ Ly α lines in this region. Comparisons to predicted values for dN/dz are not possible because of the low resolution of the data.

2. Coincidences and anticoincidences are based on lists of $5\sigma_w$ lines, and of the total 83, 85, and 102 lines for A–C, respectively, in the “Ly α -only” region, there are 72, 76, and

89 Ly α lines; the remaining lines have been identified as metals. Component D is not used for comparisons across lines of sight because of its poor SNR. For the Ly α lines there are 62, 68, and 62 coincidences for paired lines of sight AC, BC, and AB; there are 3, 1, and 1 anticoincidences. These are upper bounds to the anticoincidence rate given that each of the fitted lines in the FOS spectra comprise several components when observed at echelle resolution. There are 11, 9, and 13 metal lines identified in the “Ly α -only” region for A–C, respectively. There are 8, 9, and 8 coincidences for paired lines of sight AC, BC, and AB, and each has one anticoincidence that has been qualified as rather uncertain.

3. Scatter plots of the equivalent widths for both Ly α and the metal line pairs are highly correlated with all pairs matching within 100 km s^{-1} for the Ly α lines and 75 km s^{-1} for the metal lines (with one exception in BC having $\Delta v = 146 \text{ km s}^{-1}$). The absence of outliers indicates that if there are differences in equivalent widths between the lines of sight, it is not due to large variations in only a few lines. The scatter in the equivalent width plots for the metal lines is slightly larger than for the Ly α lines, but there are far fewer metal line pairs and their measured equivalent widths almost certainly contain some contribution from adjacent Ly α lines.

4. Histograms of the difference in equivalent width between pairs of Ly α lines ratioed to their propagated errors are slightly broader than a distribution consistent with no differences between the line pairs to within the errors. Maximum-likelihood analysis of simulated data demonstrates that the line-fitting software has underestimated the error in the equivalent widths by an amount ($\sim 46\%$) that explains the additional broadening of the real histograms, indicating that the difference detected is due to an underestimate in the measured error and probably not to any intrinsic difference in the absorption strength between the various lines of sight. This method also puts an upper limit on the average variation in rest equivalent width that would be detectable with our data, which is 0.063, 0.071, and 0.065 \AA for AC, BC, and AB and corresponds to 13%, 15%, and 14% of the average line strength. This also translates to a column density difference assuming unsaturated lines, of $\log(\Delta N_{\text{H}}) = 13.06, 12.12,$ and 13.08 , where ΔN_{H} is in cm^{-2} .

5. A continuum-fitting and line-profile independent method of determining variations in absorptivity across lines of sight shows these limits are approximately a factor of 2 smaller than those obtained by comparing the measured parameters of pairs of lines: 7.5%, 6.3%, and 8.4% for AC, BC, and AB, respectively. The corresponding column densities are $\log(\Delta N_{\text{H}}) = 12.81, 12.74,$ and 12.86 , where ΔN_{H} is in cm^{-2} .

6. The distribution of the velocity separations for AC, BC, and AB Ly α line pairs have rms 42.9, 32.1, and 28.8 km s^{-1} . The rms for the distribution of velocity differences for the metal lines are 44.5, 51.5, and 32.7 km s^{-1} , which is slightly larger than for the Ly α pairs; however, there are only a few metal line pairs and their true equivalent widths and line centers are probably more uncertain. Histograms of the velocity splittings between pairs of lines ratioed to the errors in line center (km s^{-1}) added in quadrature are also slightly broader than a distribution expected for no variations in velocity to within the errors. Maximum-likelihood analysis of the simulated data finds the errors in line centers

(km s^{-1}) have been underestimated by $\sim 42\%$, which is consistent within the errors with the detected level of broadening in the real data distributions. The upper limit on the variations in velocity for the Ly α absorbers is 47, 36, and 35 km s^{-1} for AC, BC, and AB.

5. DISCUSSION

The past few years have seen a dramatic advance in our understanding of the large numbers of low hydrogen column absorbers that make up the Ly α forest. The *Hubble Space Telescope* has allowed the distribution of absorbers to be followed down to low redshifts (Bahcall et al. 1996), where it can be compared with the galaxy distribution (Morris et al. 1993). The light gathering power of the Keck telescopes has yielded quasar spectra of unprecedented resolution and signal-to-noise (see, e.g., Hu et al. 1995; Lu et al. 1996). These observations have shown that the Ly α absorbers have significant metal enrichment and detectable clustering along the line of sight on scales of $50\text{--}100 \text{ km s}^{-1}$ (Songaila & Cowie 1996; Tytler 1995). Coincident absorption between quasar pairs shows that the coherence length of the absorbers at $z < 1$ is several hundred kpc (Dinshaw et al. 1995; Fang et al. 1996).

Our physical understanding of the absorbers has been illuminated by the supercomputer simulations that incorporate gas dynamics (Kang et al. 1994). This work reveals the shortcomings of simple models that rely on equilibrium physics and spherical symmetry. In the N -body simulations, the Ly α absorbers trace a complex filamentary web of structures (Cen et al. 1994; Hernquist et al. 1996). The simulations reveal a rich phenomenology for the gas—including free expansion, shocks, and velocity caustics (Miralda-Escudé et al. 1996). The absorption lines trace the small neutral component of a mostly ionized gas distribution, with the implication that the Ly α absorbers account for most of the baryons at high redshift. Moreover, these absorbers with low overdensities are excellent tracers of the dark matter distribution.

The four sight lines of the gravitational lens B1422+231 can be used to probe the structure of Ly α absorbers at $z \sim 3$ on transverse scales much smaller than 1 kpc. This is of course far smaller than the resolution of the best simulations. It is also far smaller than the known coherence length of the absorbers from observations of wider separation pairs. Previously, other lens systems have been used to show the homogeneity of the absorbers on different scales and at different redshifts: $\lesssim 0.24 \text{ kpc}$ at $z \sim 1.7$ for the triple quasar 1115+080 (Weymann & Foltz 1983), $\sim 5 \text{ kpc}$ at $z \sim 2$ for 2345+007A,B (Foltz et al. 1984), $\sim 1 \text{ kpc}$ at $z \sim 2.3$ for UM 673A,B (Smette et al. 1992), and $\sim 10 \text{ kpc}$ at $z \sim 2$ for HE 1104–1805 (Smette et al. 1995). In all these studies, $\sigma(\Delta v) = 15\text{--}25 \text{ km s}^{-1}$ for coincident lines, reflecting observational error rather than intrinsic scatter. We extend this work to higher redshifts and smaller scales, with constraints on models coming both from the equivalent widths and the velocities of the lines.

At $z \sim 3$ it is difficult to directly associate the absorbers with galaxies. However, at low redshifts ($z < 1$), various groups have identified bright galaxies with impact parameters of $100\text{--}300 \text{ kpc}$ from Ly α absorbers. The velocity differences at those separations are $100\text{--}200 \text{ km s}^{-1}$; some of these large velocity differences are real, but usually the dis-

tribution of Δv is dominated by observational error. Lanzetta et al. (1995) interpreted their results in terms of galaxies with gaseous halos of $\sim 160 \text{ kpc}$ extent; the absorber covering factor was in the range $0.3\text{--}0.6$. Other groups found similar associations (LeBrun, Bergeron, & Boisse 1995; Bowen, Blades, & Pettini 1996); however, they chose to interpret the absorbers as being more loosely connected with bright galaxies, perhaps with both embedded in the same large-scale structure. The absorbers with small equivalent widths can be found both near bright galaxies and in apparent voids (Morris et al. 1993; Stocke et al. 1995; van Gorkom et al. 1996).

We can interpret our lens observations in terms of three simple but astrophysically motivated models for the absorbers. The first is the idea of dense clouds confined by hot ambient gas in galactic halos. For an isotropic velocity distribution, the cloud-to-cloud velocity differences will be $\Delta v \approx (GM/R)^{1/2}$, or $100\text{--}200 \text{ km s}^{-1}$ for massive galaxies with halo radius R . This is an approximation as clouds in a halo are subject to drag forces due to the hot medium that can reduce the cloud velocity relative to the circular velocity of the halo (Mo 1994a). Mo (1994b) discussed the physical conditions of these clouds, which might arise naturally from the merger of dark-matter-dominated minihalos (Mo, Miralda-Escudé, & Rees 1993). With n_c clouds and a 50% covering factor, the radius of each cloud is $r_c = 2^{1/2}/20(n_c)^{1/2} \text{ kpc}$. Plausible models have $1 < r_c < 10 \text{ kpc}$, implying $100 < n_c < 10^4$. We therefore expect all the quasar sight lines to pierce a single cloud in most cases. In the rare cases where the sight lines pierce different clouds in the halo, a typical $\Delta v = 100\text{--}200 \text{ km s}^{-1}$ is expected. Since the fraction of anticoincidence goes as $(r_c/D)^2$, where D is the transverse separation of the lines of sight at the absorber, our small fraction of anticoincidence ($\sim 3\%$) and lack of large values of Δv imply $r_c \gtrsim 2 \text{ kpc}$ and $n_c \lesssim 800$.

The second model is a rotating disk, where the gas must be quite smoothly distributed since the absorption covering factor and the volume filling factor are similar. For randomly inclined disks with a flat rotation curve, the velocity is $v_{\text{max}}(l/r_d) \cos \alpha \sin \theta$, where $v_{\text{max}} = 100\text{--}200 \text{ km s}^{-1}$, l is the distance from the line of sight to the center of rotation, r_d is the radial distance on the disk, θ is the inclination of the disk rotation axis to the plane of the sky, and α is the angle between the line of sight and the ellipse semimajor axis. Since $D/l \ll 1$, we expect $\Delta v < 10 \text{ km s}^{-1}$ (sampling small deviations along a flat rotation curve) and $\sigma(\Delta v) < 20 \text{ km s}^{-1}$ (from the limit on z -motions in a rotating gas disk). The velocity differences therefore provide no useful constraint. The observations also give an upper limit $10\%\text{--}15\%$ on the equivalent width variations on scales of $\sim 0.1 \text{ kpc}$. Although this is less than the inhomogeneity of H I clouds in the Milky Way disk on these scales (Kulkarni & Heiles 1988), our limited resolution and ignorance of the variation in column density (due to heavy blending) limits the interpretation.

Last, we consider a simple geometry that is designed to reflect the large coherent structures seen in the supercomputer simulations. For a sheet or filament in free Hubble expansion and inclined at an angle ϕ to the line of sight, the three-dimensional separation of interception points is given by the familiar relation $r_{1,2} = (r_1^2 + r_2^2 - 2r_1r_2 \cos \alpha)^{1/2}$, where α is the angle between pairs of sight lines. The velocity difference is $\Delta v = H(z)D \tan \phi$. At the redshift and separation of the B1422+231 system,

$\Delta v \approx 0.2 \tan \phi \text{ km s}^{-1}$. The low anticoincidence rate indicates that the transverse extent of the structures is $\gg D$, and so may favor sheets over filaments. For random inclinations, most of the paired lines will have $\Delta v < 10 \text{ km s}^{-1}$, as observed, and a detectable $\Delta v \geq 50 \text{ km s}^{-1}$ will occur with negligible frequency consistent with the low observed anticoincidence rate. In this model velocity differences due to Hubble flow are undetectable on these spatial scales even at the highest obtainable resolution.

No particular geometric model is favored by these simple tests. However, the B1422+231 observations have allowed us to put a limit on the size and number of clouds in a spherical halo model, to put a limit on the clumpiness of the low column density gas in an extended disk model, and to

find satisfactory agreement with a model of freely expanding sheets or filaments. The combination of data from multiple quasars with a range of separations will be required to understand the geometry of the absorbers.

We acknowledge support from NASA under the grant GO-04402.01-92A. C. B. I. and C. B. F. acknowledge the support of the NSF grant AST 93-20715. We are grateful for help and advice from Michael Dahlem and Anuradha Koratkar, at the Space Telescope Science Institute. We have had many useful conversations and insights from Nadine Dinshaw, Neal Katz, Hans-Walter Rix, Gary Schmidt, and Ray Weymann.

APPENDIX

A1. LINE SELECTION ALGORITHM

Selection and measurement of absorption lines is performed in two phases. First, an iterative search is made for minima in the data array containing the flux values for each spectrum that has been convolved with the instrumental profile. A *primary* line list is formed from minima found in the first pass, and a *secondary* list is made from minima found in the convolved array after lines in the primary list are subtracted from the original data. The primary and secondary lists combine to form the preliminary line list, which defines an initial “best guess” at the final line list. In the second phase a region is defined about each absorption feature to which all possible combinations of primary lines within the region are fitted. The number of lines and the line parameters of the final fit must meet certain requirements in order to be accepted as the final values.

The iterative method used for initially locating and measuring lines in the spectrum of each component follows that described in detail by Paper II of the *HST* Quasar Absorption Line Key Project (Schneider et al. 1993). Essentially, the equivalent width (W) at every pixel in each spectrum is computed by centering the LSF on the i th pixel and performing the weighted sum over the 6σ limits of the Gaussian forming the array W_i . Similarly, this is done for the error array, σW_i , and the interpolated error array, $\bar{\sigma} W_i$. The interpolated error array is calculated by replacing flux errors for data points that deviate negatively by more than 2σ by the average of the errors in up to 5 (on each side) of the adjacent “continuum” points. “Continuum” in this sense is defined by points lying within a 2σ deviation from the fitted continuum. This array is different from the error array in that the errors at the centers of the lines are increased slightly to reflect the noise in the adjacent continuum. Note that the “SNR” is defined as $W_i/\sigma W_i$, whereas for our purposes here the “significance” of a line is defined as $W_i/\bar{\sigma} W_i$, which is used to select lines in the preliminary phase. This correction for the drop in the 3σ limits in the centers of lines, where the flux errors are smaller, allows for a more uniform comparison of relative line strengths.

The primary line list was generated by identifying the minima in the W_i array within a window of width one half the instrumental resolution that had a significance ($W_i/\bar{\sigma} W_i$) of 3 or more. A parabolic fit through the two adjacent points identifies the line center and the value of W_i and σW_i corresponding to this wavelength give the equivalent width and error. The profiles of the lines were calculated and subtracted from the original spectra. This subtracted spectrum was then convolved and a secondary line list was derived in the same way. The secondary list was then subtracted from the original spectrum, and a pass was made again that refits only the primary lines and may add new lines or drop existing lines. It was found experimentally that after approximately five iterations of finding lines for first the primary and then the secondary lists, the number of lines converged to a repeating series as the line centers are shifted about slightly depending on the noise. The number of lines that was added or lost is no more than a few percent of the total list. The preliminary line list was formed from the combination of the two lists, and if their profiles are subtracted from the original data array, the result has flux variations entirely consistent with noise.

A2. LINE-FITTING ALGORITHM

The combined list of lines was input as a first guess to the simultaneous best fit of each absorption feature in a spectrum. The fitting algorithm steps through each spectrum and defines the region to be fitted as beginning where the flux array downward-crosses the continuum and ending where it upward-crosses the continuum. This method of defining the fitted regions is reasonable for data of this resolution and SNR because the number of upward- and downward-crossings divides the spectrum into sections that can be fitted by a moderate number of preliminary lines (≤ 8) and limits the number of regions where no preliminary lines are found. Lines from the initial list that fall within this range were counted, n , and the number of all possible combinations of these lines, N_{comb} , was computed by summing the binomial coefficient, C_x^n , which gives the number of combinations possible for n lines taken x positions at a time, over the number of possible positions, $x = 1 \dots n$:

$$N_{\text{comb}} = \sum_{x=1}^n C_x^n = \sum_{x=1}^n \frac{n!}{x!(n-x)!}. \quad (\text{A1})$$

The member lines for each individual combination were worked out and saved, and each combination of lines was fitted simultaneously to the region following a Marquardt minimization technique that varies the amplitude and center of the lines. The line parameters and the reduced chi square (χ_v^2), which is later used to select the best fit, for each combination were saved. The method of fitting all combinations of preliminary lines optimizes selection of the best fit to any absorption feature by maximally utilizing the information provided by the preliminary line list.

Unfortunately in practice, χ_v^2 is not a sensitive test of overfitting in selecting the best fit to a region (Rauch et al. 1992). For example, it is possible for a fit to produce a χ_v^2 that is improved from the prior fit but where the errors in the equivalent width are larger than the equivalent width itself. However, the central wavelengths are fairly well determined and do not change more than a few standard deviations with subsequent fits, also the FWHM is always held constant following the assumption of unresolved lines. It is therefore helpful to impose a secondary constraint on the equivalent width to ensure the final fit consists of meaningful line parameters. The fits were examined in order of increasing χ_v^2 , and the best fit was chosen as the first one that satisfies the requirement that the error in the equivalent width of any line is not greater than 90% of the equivalent width itself. This experimentally determined criterion results in a final fit having the lowest value of χ_v^2 , while retaining reasonable values for the equivalent widths. This criterion does not have the effect of fitting many weak lines to a particular region, and the total number of weak lines in the final line lists is small. There are 3, 3, 4, and 0 lines that have significances $SL = W/\sigma_w < 3.0$, which is 2.4%, 2.3%, 2.1%, and 0% of the total line lists for A–D, respectively. Significance limits are imposed for the inclusion of lines in subsequent analyses.

In some cases the best fit from the simultaneous fitting algorithm did not result in a satisfactory χ_v^2 due to underfitting, and the pooriness of the fit was confirmed by visual inspection. Underfitting can occur because the success of this method depends on the input list of preliminary lines, and regions can be underfit by the automatic process if too few lines were chosen in the preliminary phase or if the line parameters that are chosen are not ideally suited for the minimization algorithm to find the best fit. To compensate for this weakness in the preliminary line selection algorithm, the software provides the option to interactively add extra preliminary lines. No more than two lines were ever added to any particular region and generally only one was needed. The criterion for the addition of an extra line was based on the current best-fit value of χ_v^2 . The critical value

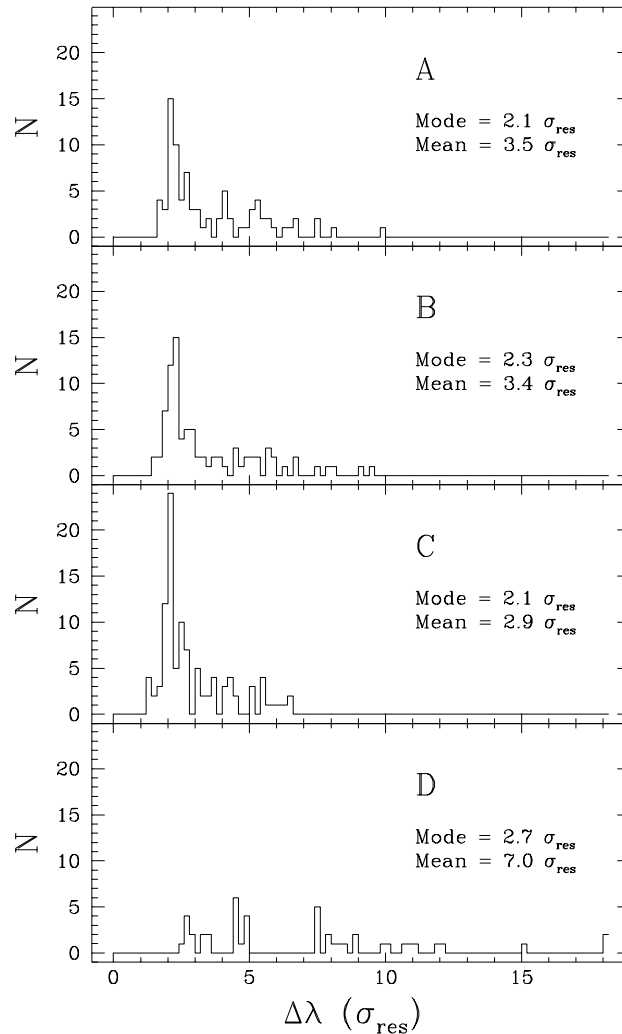


FIG. 11.—Distribution of nearest neighbor line separations for all four components. Line separation, $\Delta\lambda$, is in units of 1σ of the instrumental resolution, σ_{res} .

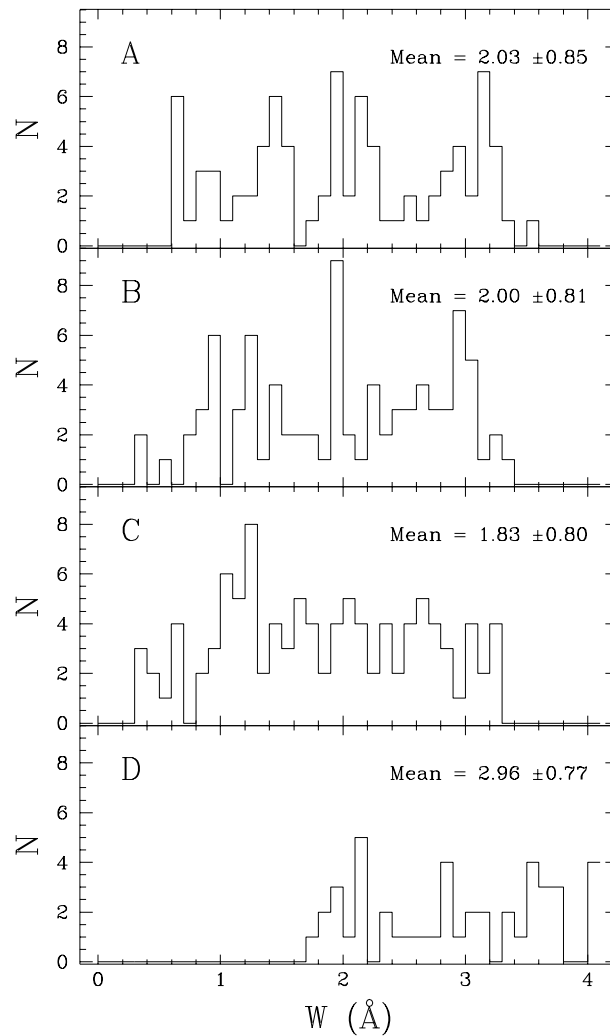


FIG. 12.—Distribution of equivalent widths measured for lines in all four lines of sight

of χ_v^2 was determined by inspection of a histogram representing the distribution of χ_v^2 obtained for each absorption line found in all four spectra by the simultaneous fitting algorithm where no intervention was made. A natural break in the distribution occurs at $\chi_v^2 \sim 5$ and this holds for χ_v^2 histograms for each component separately. This value is supported experimentally as fits with $\chi_v^2 \leq 5$ appear to be satisfactory, whereas those with $\chi_v^2 > 5$ do not. If the automatic fitting procedure resulted in a χ_v^2 of greater than 5, a preliminary line was added in the deficient region with an estimated equivalent width corresponding to a Gaussian peak at the flux at that wavelength. The number of member components of all possible combinations were recomputed, each combination is refitted to the region, and the best fit was selected according to the previously discussed rules. The total number of lines added interactively was small, 2, 8, and 8, or 1.6%, 6.1%, and 4.2% of the total lists for A, B, and C; no extra lines were added to the list for D. The χ_v^2 was improved significantly in all cases except in component C, where in three fits the additional line was not selected and the final χ_v^2 are ~ 6 , and several of the weak, single lines found redward of Ly α emission have high χ_v^2 because of the small number of pixels in the fitted regions. Visual inspection confirmed that all final fits are satisfactory.

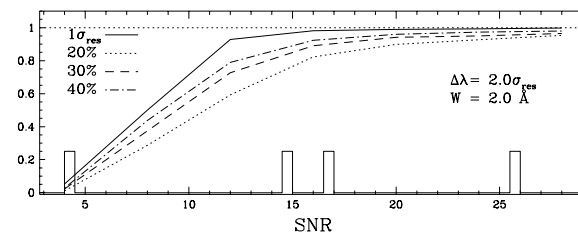


FIG. 13.—Recovery rate for one of two lines input to the simulated data having line separation $2.0\sigma_{\text{res}}$ and average equivalent width 2.0 \AA as a function of SNR. The solid line is the fraction of lines whose central wavelength was recovered to within $1\sigma_{\text{res}}$. The dotted, dashed, and dot-dashed lines are the fraction of the $1\sigma_{\text{res}}$ lines that were recovered to within 20%, 30%, and 40% of the input equivalent width, respectively. The SNR_{pix} of the four components is shown by the histogram.

TABLE 6
RECOVERY RATES FROM THE SIMULATIONS

VARIED PARAMETER (1)	PARAMETER VALUE (2)	λ_c^c $1\sigma_{\text{res}}$ (3)	EQUIVALENT WIDTH ^d		
			20% (4)	30% (5)	40% (6)
SNR	4	0.052	0.023	0.027	0.034
	16	0.98	0.89	0.92	0.94
	24	0.99	0.95	0.97	0.99
	1.5	0.63	0.28	0.37	0.42
$\Delta\lambda$ (σ_{res}) ^a	2.0	0.99	0.80	0.88	0.91
	2.5	0.99	0.95	0.97	0.98
	3.0	1.00	0.98	0.99	1.00
Ratio ^b	0.750	0.84	0.33	0.57	0.73
	0.875	0.96	0.66	0.84	0.89
	1.000	0.98	0.80	0.88	0.91

^a The separation between the simulated line pair in units of one standard deviation of the instrumental resolution ($1\sigma_{\text{res}}$).

^b The ratio of the test line equivalent width to that of the reference line ($W_{\text{ref}} = 2.0$ Å).

^c The fraction of test lines whose central wavelengths (λ_c) were recovered to within $1\sigma_{\text{res}}$.

^d The fraction of test lines from col. (3) whose equivalent widths were recovered to within the specified percentage of the input value in cols. (4)–(6).

A3. EVALUATION OF THE SOFTWARE

Because of the high density of Ly α forest lines at the redshift of B1422+231, it is useful to quantify how well the software recovers absorption lines given the SNR, line density, and resolution of the FOS data. Three simple tests were designed to cover the parameter space defined by the data. The line separation, SNR, and line strength ratio were varied for two absorption lines input to an artificial spectrum of the same dispersion and resolution of the FOS data. One thousand spectra were generated for each set of parameters in each test. The results give a general idea of the recovery reliability by varying each line parameter independently. A true estimate of the recovery reliability would require a full three-dimensional surface of simulations, and in addition, many of the lines in the real data are in highly blended regions, whereas the simulations only dealt with a pair of blended lines.

Because A and B are similar in SNR, C is much higher and D is much lower, the simulation parameters are chosen to most closely describe A and B and the results can be generalized to C and D by scaling. The distribution of line separations for

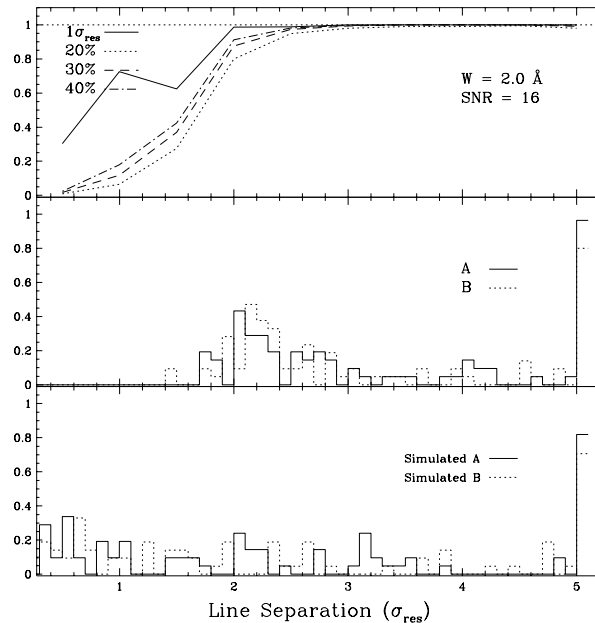


FIG. 14.—(top) Recovery rate of one of two lines input to the simulated data having average equivalent width 2.0 Å and SNR = 16 as a function of line separation, $\Delta\lambda$, in units of σ_{res} . The solid line is the fraction of lines recovered to within $1\sigma_{\text{res}}$; the dotted, dashed, and dot-dashed lines are the fraction of these lines whose equivalent widths were recovered to within 20%, 30%, and 40% of the input equivalent width, respectively. (middle) Distribution of nearest neighbor line separations for components A and B. (bottom) Distribution for a random distribution of line separations given the observed line densities for components A and B.

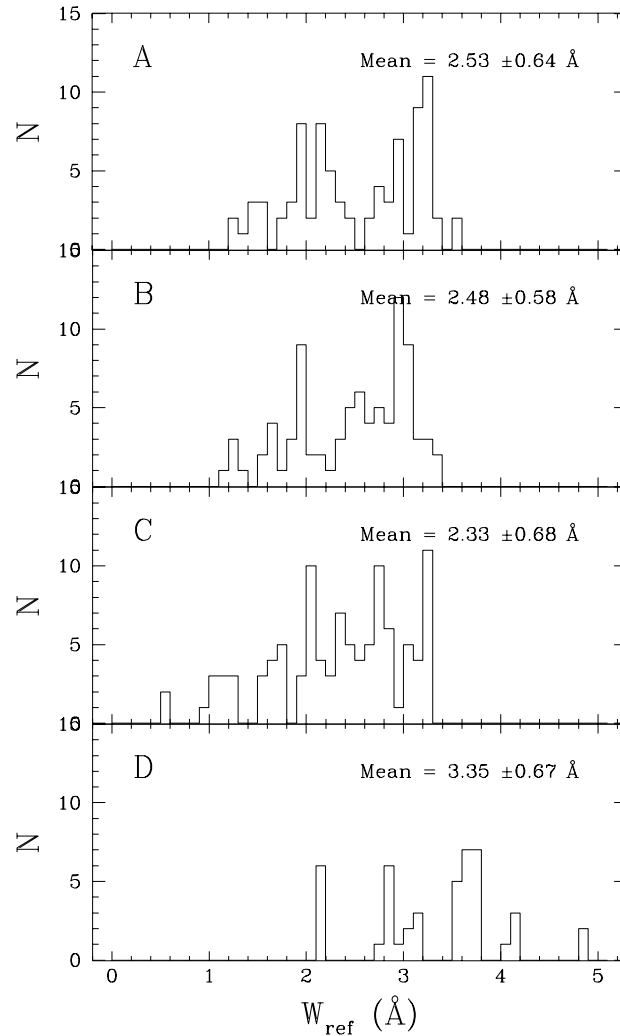


FIG. 15.—For nearest neighbor pairs in all four components, the distribution of the equivalent widths of the stronger line in the pair is plotted

nearest neighbor pairs along the line of sight in the “Ly α -only” region (as defined in § 3.1.1) for each component is shown in Figure 11. The number of lines in this region is 83, 85, 102, and 44 for A–D, respectively. For A and B the mean values are 5.93 and 5.74 Å (or $3.5\sigma_{\text{res}}$ and $3.4\sigma_{\text{res}}$). However, since the objective is a characterization of the majority of the lines, the more useful number is the mode, which is 3.55 Å or $\sim 2.0\sigma_{\text{res}}$ for both. Also for each component the distribution of equivalent widths (W) for lines in the sample region is displayed in Figure 12, and the average values for A and B are 2.03 ± 0.85 and 2.00 ± 0.81 Å. The artificial spectra are composed of two input lines having $W = 2.0$ Å with separation $\Delta\lambda = 3.34$ Å, and $\text{SNR}_{\text{pix}} = 16$, where the varied parameter takes on values in a range appropriate to span the observed data.

The first simulation examines the recovery rate of the input absorption lines as a function of SNR_{pix} to quantify the ability of the software to recover absorption lines having strength and separation similar to those of A and B. The SNR_{pix} is varied from 4 to 28 in steps of 4, which spans the range in SNR_{pix} of the spectra for the four components. The simulated spectra are degraded to the appropriate SNR and processed by the line-finding software. How well a line is recovered is measured by finding the fraction of times, when two lines are recovered, the second line reproduces the input parameters. This works equally as well if the first line is used instead. In Figure 13, the fraction of lines whose central wavelengths were recovered in this way to within $1\sigma_{\text{res}}$ is plotted as a solid line. The dashed lines represent the fraction of these lines whose equivalent widths were recovered to within 20%, 30%, and 40% of the input value. Also overplotted is a histogram representing the SNR_{pix} of the four spectra. Recovery rates for the central wavelengths and for the equivalent widths for selected parameter values are presented in Table 6. Almost all of the input line centers (98%) were recovered and their equivalent widths were recovered within 30% of the input value 92% of the time. This indicates that for components A and B, lines of the input strength and separation are well recovered in wavelength and equivalent width. These rates reflect the level of accuracy obtainable that is imposed by the S/N of the data and is not a limitation imposed by the software. These lines will be better recovered in C and for D, because the SNR is so low, the lines that are well recovered must be much stronger and more widely spaced.

In the next test the recovery rate is evaluated for one line in a pair having the typical SNR and line strength for components A and B as a function of increasing separation. The distance between the line centers was varied from $\Delta\lambda = 0.5\sigma_{\text{res}}$ to $5.0\sigma_{\text{res}}$ in steps of $0.5\sigma_{\text{res}}$ for input lines of $W = 2.0$ Å and $\text{SNR}_{\text{pix}} = 16$. The results are presented in Figure 14a with the same conventions as the first test. For comparison a histogram of the nearest neighbor pair line separation distributions for A and

B arbitrarily scaled to the fraction of total lines and multiplied by four is presented in Figure 14b. This graph indicates that for spectra having the given SNR and line strength, the software has trouble resolving lines that are closer than about $2.0\sigma_{\text{res}}$. However, it also shows that the software fitted the majority of lines in the data with separations greater than this.

The final simulation examines the effect the presence of a stronger line has on the recovery of a weaker line when the SNR_{pix} and line separation have the typical values for A and B. The ratio of the weaker neighbor line to the reference line, $W_{\text{ref}} = 2.0$ Å, was varied from $\frac{1}{8}$ to 1 in steps of an eighth. The rates at which the central wavelength and equivalent width of the weaker line were recovered are listed for selected values of the ratio in Table 6. The distribution of W_{ref} for nearest neighbor pairs along the line of sight for all four components is presented in Figure 15. The simulations show the software recovers lines reasonably well down to a pair ratio of 0.750 and cannot reliably resolve pairs with smaller ratios. However, neither A nor B have any line pairs where $W_{\text{ref}} < 2.0$ Å and $\Delta\lambda < 2.0\sigma_{\text{res}}$, and since the previous tests indicate that the software cannot reliably detect lines below these limits, this means the software is not arbitrarily fitting lines beyond these limits.

In the end, the best way to test how well the software can deblend lines at a particular SNR will be to compare the FOS line lists to the line list derived from high-resolution Keck spectra of this quasar. The simulations described above are limited because they treat the three effects of line strength, separation, and ratio separately, and only for a pair of lines; however, they can be used to describe in general the limitations of both the software and the data. Recovery rates for selected values of all three parameters are presented in Table 6. The simulations indicate that for data having resolution, dispersion and SNR comparable to A and B, the software can fairly reliably recover line pairs having SNR = 16, with $\Delta\lambda \geq 2.0\sigma_{\text{res}}$, and $W_{\text{ref}} > 2.0$ Å. This describes almost all the lines selected for A and B. While this shows the software does not fit lines outside this parameter space, it does not account for the lines that are truly present in this parameter space but are missed. The nearest neighbor line separation histogram for a random distribution of an equal number of lines found in the "Ly α -only" region for A and B is presented in Figure 14c and indicates that 43% and 54% of the lines have separation distances closer than $2.0\sigma_{\text{res}}$, or closer than the software can reliably resolve. These lines also have a random distribution of strengths, but the net effect is that two lines of close separation will be fitted by the software as a single stronger line. While it is not possible to resolve these lines, the software does fit the absorption features in a self-consistent and repeatable way, and this allows for a meaningful comparison between the measured equivalent widths.

REFERENCES

- Aldcroft, T. 1993, Ph.D. thesis, Stanford Univ.
 Bahcall, J. N., et al. 1996, *ApJ*, 457, 19
 Bechtold, J. 1994, *ApJS*, 91, 1
 Bechtold, J., Crotts, A. P. S., Duncan, R. C., & Fang, Y. 1994, *ApJ*, 437, 83
 Bechtold, J., & Yee, H. K. C. 1995, *AJ*, 110, 1984
 Bergeron, J., & Boisse, P. 1991, *A&A*, 243, 344
 Bergeron, J., et al. 1994, *ApJ*, 436, 33
 Bowen, D. V., Blades, J. C., & Pettini, M. 1996, *ApJ*, 464, 141
 Cen, R., Miralda-Escudé, J., Ostriker, J. P., & Rauch, M. 1994, *ApJ*, 437, 9
 Dinshaw, N., Impey, C. D., Foltz, C. B., Weymann, R. J., & Chaffee, F. H. 1994, *ApJ*, 437, 87
 Dinshaw, N., Impey, C. D., Foltz, C. B., Weymann, R. J., & Morris, S. L. 1995, *Nature*, 373, 223
 Dinshaw, N., Weymann, R. J., Impey, C. D., Foltz, C. B., & Ake, T. 1997, *ApJ*, in press
 Fang, Y., Duncan, R. C., Crotts, A. P. S., & Bechtold, J. 1996, *ApJ*, 462, 77
 Francis, P. J., Hewett, P. C., Foltz, C. B., Chaffee, F. H., Weymann, R. J., & Morris, S. L. 1991, *ApJ*, 373, 465
 Foltz, C. B., Weymann, R. J., Röser, H. J., & Chaffee, F. H. 1984, *ApJ*, 281, 1
 Hammer, F., Rigaut, F., Angonin-Willaime, M.-C., & Vanderriest, C. 1995, *A&A*, 298, 737
 Hernquist, L. H., Katz, N., Weinberg, D. H., & Miralda-Escudé, J. 1996, *ApJ*, 457, 51
 Hogg, D. W., & Blandford, R. D. 1994, *MNRAS*, 268, 889
 Hu, E. M., Kim, T.-S., Cowie, L. L., Songaila, A., & Rauch, M. 1995, *AJ*, 110, 1526
 Impey, C. D., Foltz, C. B., Petry, C. E., Browne, I. W. A., & Patnaik, A. R. 1996, *ApJ*, 462, L53
 Kang, H., Ostriker, J. P., Cen, R., Ryu, D., Hernquist, L., Evrard, A. E., Bryan, G. L., & Norman, M. L. 1994, *ApJ*, 430, 83
 Katz, N., Weinberg, D., & Hernquist, L. 1996, *ApJS*, 105, 19
 Koratkar, A. 1996, *STScI Instr. Sci. Rep. CAL/FOS-148*
 Kormann, R., Schneider, P., & Bartelmann, M. 1994, *A&A*, 286, 357
 Kulkarni, S. R., & Heiles, C. 1988, in *Galactic and Extragalactic Radio Astronomy*, ed. G. L. Verschuur & K. I. Kellerman (New York: Springer), 95
 Kundić, T., Hogg, D. W., Blandford, R. D., Cohen, J. G., Lubin, L. M., & Larkin, J. E. 1997, preprint astro-ph/9706169
 Lanzetta, K. M., & Bowen, D. V. 1990, *ApJ*, 357, 321
 Lanzetta, K. M., Bowen, D. V., Tytler, D., & Webb, J. K. 1995, *ApJ*, 442, 538
 Lawrence, C. R., Neugebauer, G., Weir, N., Matthews, K., & Patnaik, A. R. 1992, *MNRAS*, 259, 5
 Le Brun, V., Bergeron, J., & Boisse, P. 1995, *A&A*, 306, 691
 Lu, L., Sargent, W. L. W., Womble, D. S., & Takada-Hidai, M. 1996, *ApJ*, 472, 509
 Miralda-Escudé, J., Cen, R., Ostriker, J. P., & Rauch, M. 1996, *ApJ*, 471, 582
 Mo, H. M. 1994a, in *QSO Absorption Lines*, ed. G. Meylan (Berlin: Springer), 445
 ———. 1994b, *MNRAS*, 269, L49
 Mo, H. M., Miralda-Escudé, J., & Rees, M. J. 1993, *MNRAS*, 264, 703
 Morris, S. L., Weymann, R. J., Dressler, A., McCarthy, P. J., Smith, B. A., Terrile, R. J., Giovanelli, R., & Irwin, M. J. 1993, *ApJ*, 419, 524
 Morton, D. C., York, D. G., & Jenkins, E. B. 1988, *ApJS*, 68, 449
 Patnaik, A. R., Browne, I. W. A., Walsh, D., Chaffee, F. H., & Foltz, C. B. 1992, *MNRAS*, 259, 1
 Rauch, M., Carswell, R. F., Chaffee, F. H., Foltz, C. B., Webb, J. K., Bechtold, J., & Green, R. F. 1992, *ApJ*, 390, 387
 Remy, M., Surdej, J., Smette, A., & Claeskens, J.-F. 1993, *A&A*, 278, L19
 Sargent, W. L. W., Young, P. J., Boksenberg, A., & Tytler, D. 1980, *ApJS*, 42, 41
 Sargent, W. L. W., Young, P. J., & Schneider, D. P. 1982, *ApJ*, 256, 374
 Schneider, D. P., et al. 1993, *ApJS*, 87, 45
 Shaver, P. A., & Robertson, J. G. 1983, *ApJ*, 268, 57
 Smette, A., Surdej, J., Shaver, P. A., Foltz, C. B., Chaffee, F. H., Weymann, R. J., Williams, R. E., & Magain, P. 1992, *ApJ*, 389, 39
 Smette, A., Robertson, J. G., Shaver, P. A., Reimers, D., Wisotzki, L., & Köhler, Th. 1995, *A&AS*, 113, 199
 Songaila, A., & Cowie, L. L. 1996, *AJ*, 112, 335
 Stocke, J. T., Shull, J. M., Penton, S., Donahue, M., & Carilli, C. 1995, *ApJ*, 451, 24
 Tonry, J. L. 1997, preprint astro-ph/9706199
 Tytler, D. 1994, in *QSO Absorption Lines*, ed. G. Meylan (Berlin: Springer), 139
 van Gorkom, J. H., Carilli, C. L., Stocke, J. T., Perlman, E. S., & Shull, M. 1996, *AJ*, 112, 1397
 Weymann, R. J., Carswell, R. F., & Smith, M. G. 1981, *ARA&A*, 19, 41
 Weymann, R. J., & Foltz, C. B. 1983, *ApJ*, 272, 1
 Womble, D. S., Sargent, W. L. W., & Lyons, R. S. 1996, in *Cold Gas at High Redshift*, ed. M. Bremer et al. (Dordrecht: Kluwer), 249
 Yee, H. K. C., & Ellingson, E. 1994, *AJ*, 107, 28